Article

Estimating Lower Limb Kinematics using a Lie Group Constrained Extended Kalman Filter with a Reduced Wearable IMU Count and Distance Measurements

Luke Wicent F. Sy [1,*], Nigel H. Lovell [1] and Stephen J. Redmond [2]

[1] Graduate School of Biomedical Engineering, UNSW Sydney; l.sy@unsw.edu.au (L.S.); n.lovell@unsw.edu.au (N.L.)
[2] UCD School of Electrical and Electronic Engineering, University College Dublin; stephen.redmond@ucd.ie (S.R.)
* Correspondence: l.sy@unsw.edu.au
† This paper is an extended version of our paper entitled "Estimating Lower Limb Kinematics using a Lie Group Constrained EKF and a Reduced Wearable IMU Count" published in 2020 8th IEEE RAS/EMBS International Conference for Biomedical Robotics and Biomechatronics (BioRob); specified in the References as item 27.

Abstract: Tracking the kinematics of human movement usually requires the use of equipment that constrains the user within a room (e.g., optical motion capture systems), or requires the use of a conspicuous body-worn measurement system (e.g., inertial measurement units (IMUs) attached to each body segment). This paper presents a novel Lie group constrained extended Kalman filter to estimate lower limb kinematics using IMU and inter-IMU distance measurements in a reduced sensor count configuration. The algorithm iterates through the prediction (kinematic equations), measurement (pelvis height assumption/inter-IMU distance measurements, zero velocity update for feet/ankles, flat-floor assumption for feet/ankles, and covariance limiter), and constraint update (formulation of hinged knee joints and ball-and-socket hip joints). The knee and hip joint angle root-mean-square errors in the sagittal plane for straight walking were $7.6 \pm 2.6^\circ$ and $6.6 \pm 2.7^\circ$, respectively, while the correlation coefficients were 0.95 ± 0.03 and 0.87 ± 0.16, respectively. Furthermore, experiments using simulated inter-IMU distance measurements show that performance improved substantially for dynamic movements, even at large noise levels ($\sigma = 0.2$ m). However, further validation is recommended with actual distance measurement sensors, such as ultra-wideband ranging sensors.

Keywords: Lie group; Constrained extended Kalman filter; Gait analysis; Motion capture; Pose estimation; Wearable devices; IMU; Distance measurement

---

1. Introduction

Human pose estimation involves tracking the pose (i.e., position and orientation) of body segments, from which joint angles can be calculated. Applications exist in robotics, virtual reality, animation, and healthcare (e.g., gait analysis). Traditionally, human pose is captured within a laboratory setting using optical motion capture (OMC) systems with up to millimeter position accuracy when properly configured and calibrated. However, recent miniaturization of inertial measurements units (IMUs) has paved the path toward inertial motion capture (IMC) systems suitable for prolonged use outside of the laboratory. Furthermore, developing a comfortable IMC for routine daily use may facilitate interactive rehabilitation [1,2], and allow the study of movement disorder progression to enable predictive diagnostics.

Commercial IMCs attach one sensor per body segment (OSPS) [3], which may be considered too cumbersome and expensive for routine daily use by a consumer due to the number of IMUs required. Each IMU typically tracks the orientation of the attached body segment using an orientation estimation

Preprints (www.preprints.org) | NOT PEER-REVIEWED | Posted: 3 November 2020 doi:10.20944/preprints202011.0166.v1

algorithm (e.g., [4,5]), which is then connected via linked kinematic chain, usually rooted at the pelvis. A reduced-sensor-count (RSC) configuration, where IMUs are placed on a subset of body segments, can improve user comfort, reduce setup time and system cost. However, using fewer wearable sensor units necessarily reduces the kinematic information available, which must otherwise be inferred from (i) our knowledge of human movement (e.g., enforcing mechanical joint constraints or making dynamic balance assumptions), or (ii) by using additional sensing modalities within each wearable sensor unit. Each approach will be described in the next subsections.

1.1. Leveraging Knowledge of Human Movement

RSC performance depends on how the algorithm (i) represents body pose and (ii) infers the kinematic information of body segments which do not have sensor attached to them. The algorithm may leverage our knowledge of human movement either through data obtained in the past (i.e., observed correlations between co-movement of different body segments) or by using a simplified kinematic model of the human body. Data-driven approaches (e.g., nearest-neighbor search [6] and bi-directional recurrent neural network [7]) are able to recreate realistic motion suitable for animation-related applications. However, these approaches are normally biased toward motions already contained in the database, which may limit their use in monitoring pathological gait. Model-based approaches reconstruct body motion using kinematic and biomechanical models (e.g., linear regression [8], constrained Kalman filter (KF) [9], extended KF (EKF) [10], particle filter [11], and window-based optimization [12]). Within model-based approaches, using optimization-based estimators can be appealing due to its relative ease to setup and ease of understanding. However, it can be very inefficient in higher dimensions (e.g., when tracking body pose over a wide time window). When estimating the model state variables across time, a recursive estimator can take advantage of the substructure and reduce the state dimension, making the estimator efficient and appropriate for real-time use [13].

Traditionally, body poses have been represented using Euler angles or quaternions [10,11]. However, recent work on pose estimation has shown that using a Lie group to represent the states of recursive estimator is a promising approach. Such algorithms typically represent the body pose as a chain of linked segments using matrix Lie groups to represent the orientation or pose of each body segment; specifically the special orthogonal group, $SO(n)$, and special Euclidean group, $SE(n)$, where $n = 2, 3$, are the spatial dimensions for humam body kinematics problems. Some early work in the field ([14] and [15]) investigated representations and propagation of pose uncertainty, the former in the context of manipulator kinematics and the latter focused on $SE(3)$. This was followed by the formulation of Lie group-based recursive estimators (e.g., EKF [16] and unscented KF (UKF) [17]). Recently, Lie group based recursive estimators were used to solve the pose estimation problem. Cesic *et al*. estimated pose from marker measurements and achieved significant improvements compared to an Euler angle representation [18]; and even supplemented the approach with an observability analysis [19]. Joukov *et al*. represented pose using $SO(n)$ with measurements from IMUs under an OSPS configuration. Results also improved because the Lie group representation is singularity free [20].

1.2. Additional Sensor Measurements

Another approach is to supplement kinematic information from the IMU with another kind of sensor, which inherently increases cost and reduces battery life. Note that we will focus on systems that supplement pose estimation, not on the global position estimation of the subject (e.g., [21]). For example, IMCs can be supplemented with standard video cameras (e.g., fused using an optimization-based algorithm [22], and deep neural networks [23]) or depth cameras [24] at fixed locations in the capture environment, external to the subject. The combination of IMCs and portable cameras solves a weakness of OMCs (i.e., marker or body segment occlusion) and a weakness of IMCs (i.e., global position drift). However, the system still requires an external sensor that is

Preprints (www.preprints.org) | NOT PEER-REVIEWED | Posted: 3 November 2020 doi:10.20944/preprints202011.0166.v1

carried by another person or requires some quick setup. IMCs can also be supplemented by distance measurements (using ultrasonic devices and KF in OSPS configuration [25], using constrained KF in RSC configuration [26]), removing dependence on any external non-body-worn sensor.

1.3. Novelty

This paper describes a novel human pose estimator that uses a Lie group representation, propagated iteratively using a constrained EKF (CEKF) to estimate lower body kinematics for an RSC configuration of IMUs and inter-IMU distance measurements; the Lie group framework and inclusion of inter-IMU distance measurements, along with the exploration of its effect on pose estimation accuracy, are the major advancements made in this paper. It extends the work of [27] and builds on prior work of [9] and [26], but instead represents the state variables as elements of Lie groups, specifically $SE(3)$, to track both position and orientation (whereas [9] only tracks position and assumes orientation measurements are noise-free). Furthermore, this paper describes a novel Lie group formulation for assumptions specific to pose estimation, such as zero velocity update, and biomechanical constraints (e.g., constant thigh length and a hinged knee joint). Note that this algorithm is different from [20] in that the state (i.e., body pose) is represented as $SE(3)$ instead of $SO(n)$. While not our focus here, this representation allows for tracking of the global position of the body, incorporating IMU measurements in the prediction step, and a simpler implementation of measurement assumptions, at the cost of requiring an additional constraint step to ensure biomechanical constraints are satisfied. The design was motivated by the need for a better state variable representation which would potentially more closely model the biomechanical system to infer the missing kinematic information from uninstrumented body segments. The contributions of this paper advance the development of gait assessment tools for comfortable and long-term monitoring of lower body movement.

2. Mathematical Background: Lie Group and Lie Algebra

The matrix Lie group G is a group of $n \times n$ matrices that is also a smooth manifold (e.g., $SE(3)$). Group composition and inversion (i.e., matrix multiplication and inversion) are smooth operations. The Lie algebra $\mathfrak{g}$ represents a tangent space of a group at the identity element [28]. The elegance of Lie theory lies in it being able to represent pose using a vector space (e.g., Lie group G is represented by $\mathfrak{g}$) without additional constraints (e.g., without requiring $\mathbf{R}^T\mathbf{R} = \mathbf{I}$ which is using a rotation matrix representation of orientation, or $||\boldsymbol{q}|| = 1$ which is using a quaternion representation of orientation) [29].

The matrix exponential $\exp_G : \mathfrak{g} \to G$ (Eq. (1)) and matrix logarithm $\log_G : G \to \mathfrak{g}$ establish a local diffeomorphism between the Lie group G and its Lie algebra $\mathfrak{g}$. The Lie algebra $\mathfrak{g}$ is a $n \times n$ matrix that can be represented compactly in an n-dimensional vector space. A linear isomorphism between $\mathfrak{g}$ and $\mathbb{R}^n$ is given by operators $[\ ]_G^{\vee} : \mathfrak{g} \to \mathbb{R}^n$ and $[\ ]_G^{\wedge} : \mathbb{R}^n \to \mathfrak{g}$, which map between the compact and matrix representation of the Lie algebra $\mathfrak{g}$. Fig. 1 shows an illustration of the said mappings. Furthermore, the adjoint operator of a Lie group, $\mathrm{Ad}_G(\mathbf{X})$, the adjoint operator of a Lie algebra, $\mathrm{ad}_G(\boldsymbol{v})$, and the right jacobian, $\Phi_G(\boldsymbol{v})$ (Eq. (2)), where $\mathbf{X} \in G$ and $[\boldsymbol{v}]_G^{\wedge} \in \mathfrak{g}$ will be used in later sections. Multiplying an n-dimensional vector representation of a Lie algebra with $\mathrm{Ad}_G(\mathbf{X}) \in \mathbb{R}^{n \times n}$ (i.e., the product $\mathrm{Ad}_G(\mathbf{X})\boldsymbol{v}$) transforms the vector from one coordinate frame to another, similar to how rotation matrices transform points from one frame to another. $\mathrm{ad}_G(\boldsymbol{v})$ is the Lie algebra of $\mathrm{Ad}_G(\mathbf{X})$. A summary of the operators for Lie groups $SO(3)$, $SE(3)$, and R^n will be explained in the next subsections. They will serve as building blocks to implement the algorithm being described by this paper. For a more detailed introduction to Lie groups refer to [13,29,30].

$$\exp([\boldsymbol{v}]_G^{\wedge}) = \sum_{n=0}^{\infty} \frac{1}{n!}([\boldsymbol{v}]_G^{\wedge})^n \tag{1}$$

$$\Phi_G(\boldsymbol{v}) = \sum_{i=0}^{\infty} \frac{(-1)^i}{(i+1)!}\mathrm{ad}_G(\boldsymbol{v})^i \text{ , } \boldsymbol{v} \in \mathbb{R}^n \tag{2}$$

Preprints (www.preprints.org) | NOT PEER-REVIEWED | Posted: 3 November 2020 doi:10.20944/preprints202011.0166.v1

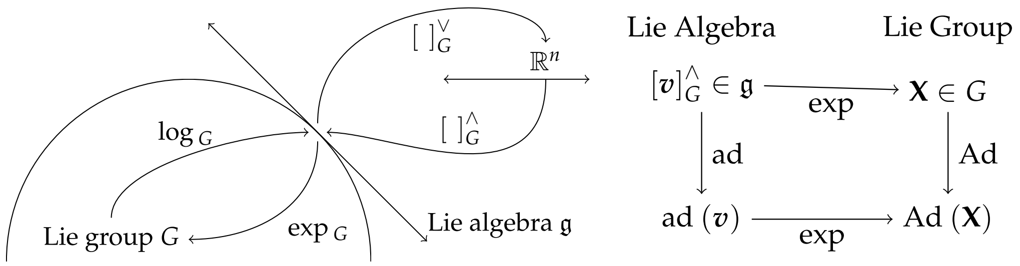

(a) Mapping between Lie group G, Lie algebra $\mathfrak{g}$, and a n-dimensional vector space.

(b) Mapping with adjoint space

Figure 1. Overview of Lie group theory mappings. When $G = SE(3)$, Lie group $\mathbf{X} = \mathbf{T}$ is a 4×4 transformation matrix representing pose (i.e., 3D rotation and translation). Similarly, $v = \boldsymbol{\xi}$ where Lie algebra $[\boldsymbol{\xi}]^\wedge_{SE(3)} \in \mathfrak{se}(3)$ and the vector $\boldsymbol{\xi} \in \mathbb{R}^n$ with $n = 6$.

2.1. Special Orthogonal Group $SO(3)$

The special orthogonal group, $SO(3) := \left\{\mathbf{R} \in \mathbb{R}^{3\times3} | \mathbf{R}\mathbf{R}^T = 1, \det \mathbf{R} = 1\right\}$, represents orientation, where $\mathbf{R}$ is the typical 3×3 rotation matrix whose column vectors represent the x, y, and z basis vectors. The operations for $SO(3)$ are listed below, and will serve as building blocks for $SE(3)$, which will be described in the next subsection. Note that $[\boldsymbol{x}]^\wedge_{SO(3)}\boldsymbol{y}$ is equivalent to the cross product of $\boldsymbol{x}$ and $\boldsymbol{y}$. See [13, Ch. 7] for details.

$$[\boldsymbol{\phi}]^\wedge_{SO(3)} = \begin{bmatrix} \phi_1 \\ \phi_2 \\ \phi_3 \end{bmatrix}^\wedge_{SO(3)} = \begin{bmatrix} 0 & -\phi_3 & \phi_2 \\ \phi_3 & 0 & -\phi_1 \\ -\phi_2 & \phi_1 & 0 \end{bmatrix}, \quad \begin{bmatrix} 0 & -\phi_3 & \phi_2 \\ \phi_3 & 0 & -\phi_1 \\ -\phi_2 & \phi_1 & 0 \end{bmatrix}^\vee_{SO(3)} = \begin{bmatrix} \phi_1 \\ \phi_2 \\ \phi_3 \end{bmatrix} = \boldsymbol{\phi} \tag{3}$$

If $\boldsymbol{\phi}/|\boldsymbol{\phi}|$ represents a unit vector axis we wish to rotate around, and $|\boldsymbol{\phi}|$ is the angle by which we wish to rotate, then the rotation matrix, $\mathbf{R}$, which will implement this rotation is given by Eq. (4), which is also known as the Rodrigues' axis-angle rotation formula. When $\boldsymbol{\phi}$ is very small, $\mathbf{R} \approx \mathbf{I}_{3\times3} + [\boldsymbol{\phi}]^\wedge_{SO(3)}$.

$$\mathbf{R} = \exp\left([\boldsymbol{\phi}]^\wedge_{SO(3)}\right) = \cos(|\boldsymbol{\phi}|)\,\mathbf{I}_{3\times3} + (1 - \cos(|\boldsymbol{\phi}|))\frac{\boldsymbol{\phi}\boldsymbol{\phi}^T}{|\boldsymbol{\phi}|^2} + \sin(|\boldsymbol{\phi}|)\left[\frac{\boldsymbol{\phi}}{|\boldsymbol{\phi}|}\right]^\wedge_{SO(3)} \tag{4}$$

Furthermore, the Lie algebra adjoint, Lie group adjoint, and inverse operators are listed in Eq. (5).

$$\mathrm{ad}_{SO(3)}(\boldsymbol{\phi}) = [\boldsymbol{\phi}]^\wedge_{SO(3)}, \quad \mathrm{Ad}_{SO(3)}(\mathbf{R}) = \mathbf{R}, \quad \mathbf{R}^{-1} = \mathbf{R}^T \tag{5}$$

Lastly, to approximate the compound rotations, $\mathbf{R}_1\mathbf{R}_2$, in the Lie algebra space where $\mathbf{R}_1 = \exp([\boldsymbol{\phi}_1]^\wedge_{SO(3)})$ and $\mathbf{R}_2 = \exp([\boldsymbol{\phi}_2]^\wedge_{SO(3)})$, we can use Eq. (6). The right Jacobian, $\Phi_{SO(3)}(\boldsymbol{\phi}) \in \mathbb{R}^{3\times3}$, is obtained using Eq. (7).

$$[\log(\mathbf{R}_1\mathbf{R}_2)]^\vee_{SO(3)} \approx \boldsymbol{\phi}_1 + \Phi_{SO(3)}(\boldsymbol{\phi}_1)^{-1}\boldsymbol{\phi}_2 \in \mathfrak{so}(3) \tag{6}$$

$$\Phi_{SO(3)}(\boldsymbol{\phi}) = \frac{\sin(|\boldsymbol{\phi}|)}{|\boldsymbol{\phi}|}\mathbf{I}_{3\times3} + \left(1 - \frac{\sin(|\boldsymbol{\phi}|)}{|\boldsymbol{\phi}|}\right)\frac{\boldsymbol{\phi}\boldsymbol{\phi}^T}{|\boldsymbol{\phi}|^2} - \frac{1-\cos(|\boldsymbol{\phi}|)}{|\boldsymbol{\phi}|}\left[\frac{\boldsymbol{\phi}}{|\boldsymbol{\phi}|}\right]^\wedge_{SO(3)} \in \mathbb{R}^{3\times3} \tag{7}$$

2.2. Special Euclidean Group, $SE(3)$

The special Euclidean group, $SE(3) := \left\{\mathbf{T} = \begin{bmatrix} \mathbf{R} & \boldsymbol{t} \\ \mathbf{0}^T & 1 \end{bmatrix} \in \mathbb{R}^{4\times4} | \{\mathbf{R}, \boldsymbol{t}\} \in SO(3) \times \mathbb{R}^3\right\}$, represents orientation and translation, where $\mathbf{T}$ is the typical 4×4 transformation matrix, $\mathbf{R}$ is the rotation matrix,

Preprints (www.preprints.org) | NOT PEER-REVIEWED | Posted: 3 November 2020 doi:10.20944/preprints202011.0166.v1

and $\boldsymbol{t}$ represents a coordinate point in Euclidean space. The operations for $SE(3)$ are listed below. $\mathbf{I}_{i\times i}$ and $\mathbf{0}_{i\times j}$ denote $i \times i$ identity and $i \times j$ zero matrices. See [13, Ch. 7] for details.

$$[\xi]^{\wedge}_{SE(3)} = \begin{bmatrix}\boldsymbol{\rho}\\ \boldsymbol{\phi}\end{bmatrix}^{\wedge}_{SE(3)} = \begin{bmatrix}[\boldsymbol{\phi}]^{\wedge}_{SO(3)} & \boldsymbol{\rho}\\ \mathbf{0}_{1\times 3} & 0\end{bmatrix}, \quad \begin{bmatrix}[\boldsymbol{\phi}]^{\wedge}_{SO(3)} & \boldsymbol{\rho}\\ \mathbf{0}_{1\times 3} & 0\end{bmatrix}^{\vee}_{SE(3)} = \begin{bmatrix}\boldsymbol{\rho}\\ \boldsymbol{\phi}\end{bmatrix} \tag{8}$$

$$\mathbf{T} = \exp([\xi]^{\wedge}_{SE(3)}) = \begin{bmatrix}\exp([\boldsymbol{\phi}]^{\wedge}_{SO(3)}) & \Phi_{SO(3)}(-\boldsymbol{\phi})\boldsymbol{\rho}\\ \mathbf{0}_{1\times 3} & 1\end{bmatrix} = \begin{bmatrix}\mathbf{R} & \boldsymbol{t}\\ \mathbf{0}_{1\times 3} & 1\end{bmatrix} \tag{9}$$

$$\mathrm{ad}_{SE(3)}(\xi) = \begin{bmatrix}[\boldsymbol{\phi}]^{\wedge}_{SO(3)} & [\boldsymbol{\rho}]^{\wedge}_{SO(3)}\\ \mathbf{0}_{3\times 3} & [\boldsymbol{\phi}]^{\wedge}_{SO(3)}\end{bmatrix}, \; \mathrm{Ad}_{SE(3)}(\mathbf{T}) = \begin{bmatrix}\mathbf{R} & [\boldsymbol{\rho}]^{\wedge}_{SO(3)}\mathbf{R}\\ \mathbf{0}_{3\times 3} & \mathbf{R}\end{bmatrix}, \; \mathbf{T}^{-1} = \begin{bmatrix}\mathbf{R}^T & -\mathbf{R}^T\boldsymbol{\rho}\\ \mathbf{0}_{1\times 3} & 1\end{bmatrix} \tag{10}$$

Lastly, we note the useful identity defined in Eq. (11) where $[\boldsymbol{a}]^{\wedge}_{SE(3)}, [\boldsymbol{b}]^{\wedge}_{SE(3)} \in \mathfrak{se}(3)$ which is the Lie algebra of the Lie Group $SE(3)$ [13, Eq. (72)], which will be used to compute the Jacobians of our model later.

$$[\boldsymbol{a}]^{\wedge}_{SE(3)}\,\boldsymbol{b} = [\boldsymbol{b}]^{\odot}_{SE(3)}\,\boldsymbol{a}, \text{ where } \boldsymbol{b} = \begin{bmatrix}\boldsymbol{\epsilon}\\ \eta\end{bmatrix}, \; [\boldsymbol{b}]^{\odot} = \begin{bmatrix}\eta\mathbf{I}_{3\times 3} & -[\boldsymbol{\epsilon}]^{\wedge}_{SO(3)}\\ \mathbf{0}_{1\times 3} & \mathbf{0}_{1\times 3}\end{bmatrix}, \; \boldsymbol{\epsilon} \in \mathbb{R}^3, \; \eta \in \mathbb{R} \tag{11}$$

2.3. Real Numbers $\mathbb{R}^n$

In order to represent vector state variables (e.g., translation, velocity, and acceleration) and be consistent with how we used $SE(3)$ to represent pose, we represented the real numbers $\boldsymbol{s} \in \mathbb{R}^n$ as $SE(n)$ poses with position and no rotation. The operations for $\mathbb{R}^n$ are listed below.

$$[\boldsymbol{s}]^{\wedge}_{\mathbb{R}^n} = \begin{bmatrix}\mathbf{0}_{n\times n} & \boldsymbol{s}\\ \mathbf{0}_{1\times n} & 0\end{bmatrix}, \quad \begin{bmatrix}\mathbf{0}_{n\times n} & \boldsymbol{s}\\ \mathbf{0}_{1\times n} & 0\end{bmatrix}^{\vee}_{\mathbb{R}^n} = \boldsymbol{s} \tag{12}$$

$$\mathbf{S} = \exp([\boldsymbol{s}]^{\wedge}_{\mathbb{R}^n}) = \begin{bmatrix}\mathbf{I}_{n\times n} & \boldsymbol{s}\\ \mathbf{0}_{1\times n} & 1\end{bmatrix}, \quad \left[\log\left(\begin{bmatrix}\mathbf{I}_{n\times n} & \boldsymbol{s}\\ \mathbf{0}_{1\times n} & 1\end{bmatrix}\right)\right]^{\vee}_{\mathbb{R}^n} = \boldsymbol{s}, \quad \exp([\boldsymbol{s}]^{\wedge}_{\mathbb{R}^n})^{-1} = \begin{bmatrix}\mathbf{I}_{n\times n} & -\boldsymbol{s}\\ \mathbf{0}_{1\times n} & 1\end{bmatrix} \tag{13}$$

$$\mathrm{ad}_{\mathbb{R}^n}(\boldsymbol{s}) = \mathbf{0}_{n\times n}, \quad \mathrm{Ad}_{\mathbb{R}^n}(\mathbf{S}) = \mathbf{I}_{n\times n}, \quad \Phi_{\mathbb{R}^n}(\boldsymbol{s}) = \mathbf{0}_{n\times n} \tag{14}$$

Note that the multiplication of two elements of the Lie group (i.e., the exponential of $\boldsymbol{s}_1$ and $\boldsymbol{s}_2$) is equivalent to the vector addition of two elements of the Lie algebra (i.e., $\boldsymbol{s}_1 + \boldsymbol{s}_2$).

$$\left[\log\left(\exp([\boldsymbol{s}_1]^{\wedge}_{\mathbb{R}^n})\exp([\boldsymbol{s}_2]^{\wedge}_{\mathbb{R}^n})\right)\right]^{\vee}_{\mathbb{R}^n} = \boldsymbol{s}_1 + \boldsymbol{s}_2 \tag{15}$$

3. Algorithm Description

The proposed algorithm, *L5S-3IMU*, uses a similar model and assumptions to our prior works in [9] and [26], denoted as *CKF-3IMU*, albeit expressed in Lie group representation, to estimate the orientation of the pelvis, thighs, and shanks with respect the world frame, W, using three IMUs attached at the sacrum and shanks, just above the ankles, and inter-IMU distance measurements (Fig. 2). Using a Lie group representation enables the tracking of not just position but also of orientation (note that *CKF-3IMU* only tracked position and assumed orientation measurements were noise-free). Fig. 3 shows an overview of the proposed algorithm. *L5S-3IMU* predicts the shank and pelvis positions through double integration of their linear 3D acceleration (obtained after a pre-processing step of IMU measurements), and predicts the shank and pelvis orientation through integration of their linear 3D angular velocity. Orientation is also further updated using a third party orientation estimation algorithm. Positional drift due to sensor noise that accumulates in the double integration of acceleration was mitigated through the following assumptions: (1) the ankle 3D velocity and height above the floor are zeroed whenever a footstep is detected; (2) the pelvis position is approximated as the length of the unbent leg(s) above the floor or as informed by inter-IMU distance measurements, when available.

Furthermore, to contain the ever-growing error covariance for the pelvis and ankle global positions, a pseudo-measurement equal to the current pose estimate with a fixed covariance is made. Lastly, biomechanical constraints enforce constant body segment lengths; and hinged knee joints (one degree of freedom (DOF)) with limited range of motion (ROM). The pre- and post-processing parts remain exactly the same as the *CKF-3IMU* algorithm.

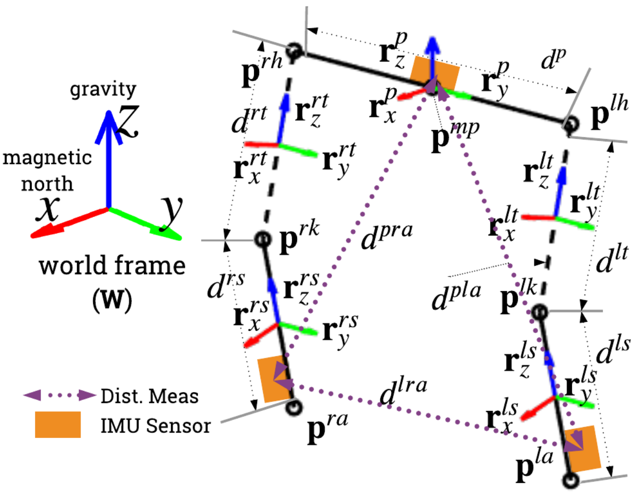

	Symbol	Description
Points/Joints	mp	mid-pelvis
	lh	left hip
	rh	right hip
	lk	left knee
	rk	right knee
	la	left ankle
	ra	right ankle
Segments	p	pelvis
	lt	left thigh
	rt	right thigh
	ls	left shank
	rs	right shank
Dist.	pla	pelvis to left ankle
	pra	pelvis to right ankle
	lra	left to right ankle

Figure 2. Model of the lower body used by LGKF-3IMU. The circles denote joint positions, the solid lines denote instrumented body segments, whilst the dashed lines denote segments without IMUs attached (i.e., thighs). Dotted lines denote inter-IMU measurements.

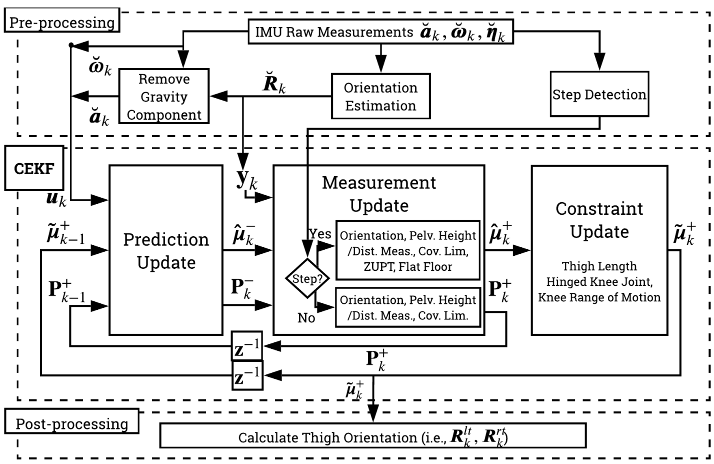

Figure 3. Algorithm overview which consists of pre-processing, CEKF, and post-processing. Pre-processing calculates the body segment orientation, inertial body acceleration, and step detection from raw acceleration, $\breve{\boldsymbol{a}}_k$, angular velocity, $\breve{\boldsymbol{\omega}}_k$, and magnetic north heading, $\breve{\boldsymbol{\eta}}_k$, measured by the IMU. The CEKF-based state estimation consists of a prediction (kinematic equation), measurement (orientation, pelvis height/inter-IMU distance measurement, covariance limiter, intermittent zero-velocity update, and flat-floor assumption), and constraint update (thigh length, hinge knee joint, and knee range of motion). Post-processing calculates the left and right thigh orientations, $\boldsymbol{R}_k^{lt}$ and $\boldsymbol{R}_k^{rt}$.

3.1. System, Measurement, and Constraint Models

The system, measurement, and constraint models are presented below

$$\boldsymbol{X}_k = f(\boldsymbol{X}_{k-1}, \boldsymbol{n}_{k-1}) = \boldsymbol{X}_{k-1} \exp([\Omega(\boldsymbol{X}_{k-1}, \boldsymbol{u}_{k-1}) + \boldsymbol{n}_{k-1}]_G^{\wedge}) \tag{16}$$

Preprints (www.preprints.org) | NOT PEER-REVIEWED | Posted: 3 November 2020 doi:10.20944/preprints202011.0166.v1

$$\mathbf{Z}_k = h(\mathbf{X}_k)\exp([\boldsymbol{m_k}]_G^\wedge), \quad \mathbf{D}_k = c(\mathbf{X}_k) \tag{17}$$

where k is the time step. $\mathbf{X}_k \in G$ is the system state, an element of state Lie group G. $\Omega\left(\mathbf{X}_k, \boldsymbol{u}_{k-1}\right) : G \to \mathbb{R}^p$ is a non-linear function which describes how the model acts on the state and input, $\boldsymbol{u}_{k-1}$, where p is the number of dimensions of the compact vector representation for Lie algebra $\mathfrak{g}$. $\boldsymbol{n}_k$ is a zero-mean process noise vector with covariance matrix $\mathcal{Q}$ (i.e., $\boldsymbol{n}_k \sim \mathcal{N}_{\mathbb{R}^p}(\mathbf{0}_{p\times 1}, \mathcal{Q})$). $\mathbf{Z}_k \in G_m$ is the system measurement, an element of the measurement Lie group G_m. $h\left(\mathbf{X}_k\right) : G \to G_m$ is the measurement function. $\boldsymbol{m}_k$ is a zero-mean measurement noise vector with covariance matrix $\mathcal{R}_k$ (i.e., $\boldsymbol{m}_k \sim \mathcal{N}_{\mathbb{R}^q}(\mathbf{0}_{q\times 1}, \mathcal{R}_k)$ where q is the number of dimensions of available measurements). $\mathbf{D}_k \in G_c$ is the constraint state, an element of constraint Lie group G_c. $c\left(\mathbf{X}_k\right) : G \to G_c$ is the equality constraint function the state $\mathbf{X}_k$ must satisfy (i.e., $c\left(\mathbf{X}_k\right) = \mathbf{D}_k$). Similar to [18,31], the state distribution of $\mathbf{X}_k$ is assumed to be a concentrated Gaussian distribution on Lie groups (i.e., $\mathbf{X}_k = \boldsymbol{\mu}_k \exp_G [\boldsymbol{\epsilon}]_G^\wedge$, where $\boldsymbol{\mu}_k$ is the mean of $\mathbf{X}_k$ and Lie algebra error $\boldsymbol{\epsilon} \sim \mathcal{N}_{\mathbb{R}^p}(\mathbf{0}_{p\times 1}, \mathbf{P})$) [14].

The Lie group state variables $\mathbf{X}_k$ model the position, orientation, and velocity of the three instrumented body segments (i.e., pelvis and shanks) as $\mathbf{X}_k = \text{diag}(\boldsymbol{T}^p, \boldsymbol{T}^{ls}, \boldsymbol{T}^{rs}, \exp([[(\boldsymbol{v}^p)^T\ (\boldsymbol{v}^{ls})^T\ (\boldsymbol{v}^{rs})^T]^T]^\wedge_{\mathbb{R}^9})) \in G = SE(3)^3 \times \mathbb{R}^9$ where $\boldsymbol{T}^b \in SE(3)$ represents the pose (i.e., orientation and position) of body segment b relative to world frame W, and ${}^A\boldsymbol{v}^b$ is the velocity of body segment b relative to frame A. If frame A is not specified, assume reference to the world frame, W. The Lie algebra error is denoted as $\epsilon = [(\boldsymbol{\epsilon}^p_{\mathbf{T}})^T\ (\boldsymbol{\epsilon}^{ls}_{\mathbf{T}})^T\ (\boldsymbol{\epsilon}^{rs}_{\mathbf{T}})^T\ (\boldsymbol{\epsilon}^{mp}_{\boldsymbol{v}})^T\ (\boldsymbol{\epsilon}^{la}_{\boldsymbol{v}})^T\ (\boldsymbol{\epsilon}^{ra}_{\boldsymbol{v}})^T]^T$ where the first three variables correspond to the Lie group in $SE(3)$ while the latter three are for $\mathbb{R}^9$. $[\,]^\vee_G$, $\exp([\,]^\wedge_G)$, $[\log(\,)]^\vee_G$, $\text{Ad}_G(\mathbf{X}_k)$, and $\Phi_G(\,)$ are constructed similarly as $\mathbf{X}_k$ (e.g., $\text{Ad}_G(\mathbf{X}_k) = \text{diag}(\text{Ad}_{SE(3)}(\boldsymbol{T}^p), \text{Ad}_{SE(3)}(\boldsymbol{T}^{ls}), \text{Ad}_{SE(3)}(\boldsymbol{T}^{rs}), \text{Ad}_{\mathbb{R}^9}(\exp([[(\boldsymbol{v}^p)^T\ (\boldsymbol{v}^{ls})^T\ (\boldsymbol{v}^{rs})^T]^T]^\wedge_{\mathbb{R}^9})))$. Refer to Sec. 2.2 and 2.3 for definition of $SE(3)$ and $\mathbb{R}^n$ operators.

3.2. Lie Group Constrained EKF (LG-CEKF)

The *a priori*, *a posteriori*, and constrained state estimate (i.e., estimated mean of $\mathbf{X}_k$) for time step k are denoted by $\hat{\boldsymbol{\mu}}_k^-$, $\hat{\boldsymbol{\mu}}_k^+$, and $\tilde{\boldsymbol{\mu}}_k^+$, respectively. Note that the true state $\mathbf{X}_k$ can be expressed as $\boldsymbol{\mu}_k \exp([\boldsymbol{\epsilon}]_G^\wedge)$ where $\boldsymbol{\mu}_k$ is one of the state means just mentioned with error, $[\boldsymbol{\epsilon}]_G^\wedge$. The *a priori* and *a posteriori* error covariance matrices are denoted as $\mathbf{P}_k^-$ and $\mathbf{P}_k^+$, respectively. Note the error covariance is not updated at the constrain update step. The KF is based on the Lie group EKF, as defined in [31], where the state means ($\hat{\boldsymbol{\mu}}_k^-$, $\hat{\boldsymbol{\mu}}_k^+$, and $\tilde{\boldsymbol{\mu}}_k^+$) and state error covariance matrices ($\mathbf{P}_k^-$ and $\mathbf{P}_k^+$) are propagated by the KF at each time step.

3.2.1. Prediction Step

Prediction step estimates the *a priori* state $\hat{\boldsymbol{\mu}}_k^-$ at the next time step and may not necessarily respect the kinematic constraints of the body, so joints may become dislocated after this step. The mean propagation of the three instrumented body segments is governed by Eq. (18) where $\Omega(\tilde{\boldsymbol{\mu}}_{k-1}^+, \boldsymbol{u}_k)$ (Eqs. (19)) is the motion model for the three instrumented body segments. The input $\boldsymbol{u}_k$ is defined in Eq. (20), where the orientation and acceleration as obtained by the IMU attached to segment b with respect world frame W are denoted as $\breve{\boldsymbol{R}}_k^b$ and $\breve{\boldsymbol{a}}_k^b$ for $b \in \{p, ls, rs\}$, while the angular velocity as obtained by the IMU attached to segment b expressed in frame b is denoted as ${}^b\breve{\boldsymbol{\omega}}_k$.

$$\hat{\boldsymbol{\mu}}_k^- = \tilde{\boldsymbol{\mu}}_{k-1}^+ \exp([\Omega(\tilde{\boldsymbol{\mu}}_{k-1}^+, \boldsymbol{u}_k)]_G^\wedge) \tag{18}$$

$$\begin{aligned}\Omega(\tilde{\boldsymbol{\mu}}_{k-1}^+, \boldsymbol{u}_k) = \Big[&\underbrace{(\Delta t\, \tilde{\boldsymbol{v}}_{k-1}^{mp+} + \tfrac{\Delta t^2}{2}\, \breve{\boldsymbol{a}}_k^p)^T\, \breve{\boldsymbol{R}}_k^p}_{1\times 3}\ \ \underbrace{\Delta t\, {}^p\breve{\boldsymbol{\omega}}_k^T}_{1\times 3}\ \ \underbrace{(\Delta t\, \tilde{\boldsymbol{v}}_{k-1}^{la+} + \tfrac{\Delta t^2}{2}\, \breve{\boldsymbol{a}}_k^{ls})^T\, \breve{\boldsymbol{R}}_k^{ls}}_{1\times 3}\ \ \underbrace{\Delta t\, {}^{ls}\breve{\boldsymbol{\omega}}_k^T}_{1\times 3}\\ &\underbrace{(\Delta t\, \tilde{\boldsymbol{v}}_{k-1}^{ra+} + \tfrac{\Delta t^2}{2}\, \breve{\boldsymbol{a}}_k^{rs})^T\, \breve{\boldsymbol{R}}_k^{rs}}_{1\times 3}\ \ \underbrace{\Delta t\, {}^{rs}\breve{\boldsymbol{\omega}}_k^T}_{1\times 3}\ \ \underbrace{\Delta t(\breve{\boldsymbol{a}}_k^{mp})^T\ \ \Delta t(\breve{\boldsymbol{a}}_k^{la})^T\ \ \Delta t(\breve{\boldsymbol{a}}_k^{ra})^T}_{1\times 9}\Big]^T\end{aligned} \tag{19}$$

$$\boldsymbol{u}_k = \begin{bmatrix} \breve{\boldsymbol{R}}_k^p & \breve{\boldsymbol{R}}_k^{ls} & \breve{\boldsymbol{R}}_k^{rs} & \breve{\boldsymbol{a}}_k^p & \breve{\boldsymbol{a}}_k^{ls} & \breve{\boldsymbol{a}}_k^{rs} & {}^p\breve{\boldsymbol{\omega}}_k & {}^{ls}\breve{\boldsymbol{\omega}}_k & {}^{rs}\breve{\boldsymbol{\omega}}_k \end{bmatrix} \tag{20}$$

Preprints (www.preprints.org) | NOT PEER-REVIEWED | Posted: 3 November 2020 doi:10.20944/preprints202011.0166.v1

The state error covariance matrix propagation is governed by Eq. (21), where $\mathcal{F}_k$ represents the matrix Lie group equivalent to the Jacobian of $f(\mathbf{X}_{k-1}, \boldsymbol{n}_{k-1})$, $\mathcal{Q}$ is the covariance matrix of the process noise, and $\mathscr{C}_k = \frac{\partial}{\partial \epsilon}\Omega(\tilde{\boldsymbol{\mu}}^+_{k-1}\exp([\epsilon]^\wedge_G), \boldsymbol{u}_k)|_{\epsilon=0}$ represents the linearization of the motion model with an infinitesimal perturbation ϵ. The process noise covariance matrix, $\mathcal{Q}$, is calculated from the input-to-state matrix $\mathcal{G}$ and the noise variances of the measured acceleration and angular velocity, σ_a^2 and σ_ω^2, respectively.

$$\mathbf{P}^-_k = \mathcal{F}_k \mathbf{P}^+_{k-1}\mathcal{F}^T_k + \Phi_G(\Omega(\tilde{\boldsymbol{\mu}}^+_{k-1}, \boldsymbol{u}_k))\mathcal{Q}\Phi_G(\Omega(\tilde{\boldsymbol{\mu}}^+_{k-1}, \boldsymbol{u}_k))^T \tag{21}$$

$$\mathcal{F}_k = \mathrm{Ad}_G(\exp_G(-[\Omega(\tilde{\boldsymbol{\mu}}^+_{k-1}, \boldsymbol{u}_k)]^\wedge_G)) + \Phi_G(\Omega(\tilde{\boldsymbol{\mu}}^+_{k-1}, \boldsymbol{u}_k))\mathscr{C}_k \tag{22}$$

$$\mathcal{Q} = \mathcal{G}\,\mathrm{diag}(\sigma_a^2, \sigma_\omega^2)\,\mathcal{G}^T \tag{23}$$

$$\begin{aligned}\mathscr{C}_k &= \tfrac{\partial}{\partial \epsilon}\Omega(\tilde{\boldsymbol{\mu}}^+_{k-1}\exp([\epsilon]^\wedge_G), \boldsymbol{u}_k)|_{\epsilon=0} \\ &= \tfrac{\partial}{\partial \epsilon}\Big[\ (\Delta t(\tilde{\boldsymbol{v}}^{mp+}_{k-1} + \boldsymbol{\epsilon}^{mp}_{\boldsymbol{v}}) + \tfrac{\Delta t^2}{2}\,\breve{\boldsymbol{a}}^p_k)^T\,\breve{\boldsymbol{R}}^p_k \;\vdots\; \Delta t\,{}^p\breve{\boldsymbol{\omega}}^T_k \;\vdots\; (\Delta t(\tilde{\boldsymbol{v}}^{la+}_{k-1} + \boldsymbol{\epsilon}^{la}_{\boldsymbol{v}}) + \tfrac{\Delta t^2}{2}\,\breve{\boldsymbol{a}}^{ls}_k)^T\,\breve{\boldsymbol{R}}^{ls}_k \;\vdots\; \Delta t\,{}^{ls}\breve{\boldsymbol{\omega}}^T_k \\ &\qquad (\Delta t(\tilde{\boldsymbol{v}}^{ra+}_{k-1} + \boldsymbol{\epsilon}^{ra}_{\boldsymbol{v}}) + \tfrac{\Delta t^2}{2}\,\breve{\boldsymbol{a}}^{rs}_k)^T\,\breve{\boldsymbol{R}}^{rs}_k \;\vdots\; \Delta t\,{}^{rs}\breve{\boldsymbol{\omega}}^T_k \;\vdots\; \Delta t(\breve{\boldsymbol{a}}^{mp}_k)^T \;\vdots\; \Delta t(\breve{\boldsymbol{a}}^{la}_k)^T \;\vdots\; \Delta t(\breve{\boldsymbol{a}}^{ra}_k)^T\ \Big]^T\Big|_{\epsilon=0} \\ \mathscr{C}_k &= \left[\begin{array}{c|ccc} & \Delta t(\breve{\boldsymbol{R}}^p_k)^T & \mathbf{0}_{3\times3} & \mathbf{0}_{3\times3} \\ & \mathbf{0}_{3\times3} & \mathbf{0}_{3\times3} & \mathbf{0}_{3\times3} \\ & \mathbf{0}_{3\times3} & \Delta t(\breve{\boldsymbol{R}}^{ls}_k)^T & \mathbf{0}_{3\times3} \\ \mathbf{0}_{18\times18} & \mathbf{0}_{3\times3} & \mathbf{0}_{3\times3} & \mathbf{0}_{3\times3} \\ & \mathbf{0}_{3\times3} & \mathbf{0}_{3\times3} & \Delta t(\breve{\boldsymbol{R}}^{rs}_k)^T \\ & \mathbf{0}_{3\times3} & \mathbf{0}_{3\times3} & \mathbf{0}_{3\times3} \\ \hline \multicolumn{4}{c}{\mathbf{0}_{9\times27}} \end{array}\right]\end{aligned} \tag{24}$$

$$\mathcal{G} = \left[\begin{array}{ccc|ccc} \Delta t^2/2\,\mathbf{I}_{3\times3} & \mathbf{0}_{3\times3} & \mathbf{0}_{3\times3} & \mathbf{0}_{3\times3} & \mathbf{0}_{3\times3} & \mathbf{0}_{3\times3} \\ \mathbf{0}_{3\times3} & \mathbf{0}_{3\times3} & \mathbf{0}_{3\times3} & \Delta t\mathbf{I}_{3\times3} & \mathbf{0}_{3\times3} & \mathbf{0}_{3\times3} \\ \mathbf{0}_{3\times3} & \Delta t^2/2\,\mathbf{I}_{3\times3} & \mathbf{0}_{3\times3} & \mathbf{0}_{3\times3} & \mathbf{0}_{3\times3} & \mathbf{0}_{3\times3} \\ \mathbf{0}_{3\times3} & \mathbf{0}_{3\times3} & \mathbf{0}_{3\times3} & \mathbf{0}_{3\times3} & \Delta t\mathbf{I}_{3\times3} & \mathbf{0}_{3\times3} \\ \mathbf{0}_{3\times3} & \mathbf{0}_{3\times3} & \Delta t^2/2\,\mathbf{I}_{3\times3} & \mathbf{0}_{3\times3} & \mathbf{0}_{3\times3} & \mathbf{0}_{3\times3} \\ \mathbf{0}_{3\times3} & \mathbf{0}_{3\times3} & \mathbf{0}_{3\times3} & \mathbf{0}_{3\times3} & \mathbf{0}_{3\times3} & \Delta t\mathbf{I}_{3\times3} \\ \hline \multicolumn{3}{c|}{\Delta t\mathbf{I}_{9\times9}} & \multicolumn{3}{c}{\mathbf{0}_{9\times9}} \end{array}\right] \tag{25}$$

3.2.2. Measurement Update

Measurement update estimates the state at the next time step by: (i) updating the orientation state using new orientation measurements of body segments from IMUs; by (ii) encouraging pelvis position to be above the feet, as informed by either some pseudo-measurement or inter-IMU distance measurements; and by (iii) enforcing ankle velocity to reach zero, and the ankle z position to be near the floor level, z_f when step is detected. When only IMU measurements are available, (iia) pelvis z position is encouraged to be close to initial standing height, z_p. When inter-IMU distance measurements are available, (iia) is not used. Instead, (iib) ankle distance is directly incorporated while pelvis position is inferred from inter-IMU distance measurements assuming hinged knee joints and constant body segment lengths. The *a posteriori* state mean $\hat{\boldsymbol{\mu}}^+_k$ is calculated following the Lie EKF equations below. Note that $[\log(h(\hat{\boldsymbol{\mu}}^-_k)^{-1}\mathbf{Z}_k)]^\vee_{G_m}$ in Eq. (27) is akin to the KF innovation/residual, where $h(\hat{\boldsymbol{\mu}}^-_k)^{-1}\mathbf{Z}_k$ (derived from Eq. (17) assuming $\boldsymbol{m}_k = \mathbf{0}$ and $\mathbf{X}_k = \hat{\boldsymbol{\mu}}^-_k$, i.e., $\mathbf{Z}_k = h(\hat{\boldsymbol{\mu}}^-_k)$) is the innovation/residual in Lie group G_m brought to the vector representation of the Lie algebra space using the inverse exponential (i.e., logarithm) mapping.

$$\hat{\boldsymbol{\mu}}^+_k = \hat{\boldsymbol{\mu}}^-_k \exp_G([\boldsymbol{\nu}_k]^\wedge_G) \tag{26}$$

$$\boldsymbol{\nu}_k = \mathbf{K}_k([\log(h(\hat{\boldsymbol{\mu}}^-_k)^{-1}\mathbf{Z}_k)]^\vee_{G_m}) \tag{27}$$

$$\mathbf{K}_k = \mathbf{P}^-_k \mathcal{H}^T_k(\mathcal{H}_k\mathbf{P}^-_k\mathcal{H}^T_k + \mathcal{R}_k)^{-1} \tag{28}$$

$\mathcal{H}_k$ can be seen as the matrix Lie group equivalent to the Jacobian of $h(\mathbf{X}_k)$, and is defined as the concatenation of $\mathcal{H}_{ori}$ and $\mathcal{H}_{mp,k}$ when inter-IMU distance measurement is not available. When inter-IMU distance measurement is available, $\mathcal{H}_{mp,k}$ is replaced by $\mathcal{H}_{dist,k} = [\mathcal{H}_{pla,k}^T \quad \mathcal{H}_{pra,k}^T \quad \mathcal{H}_{lra,k}^T]^T$. $\mathcal{H}_{ls,k}$ and/or $\mathcal{H}_{rs,k}$ are also concatenated to $\mathcal{H}_k$ when the left and/or right foot contact (FC) is detected (See [9, Eq. (9)]). Each component matrix will be described later. The measurement matrix $\mathbf{Z}_k \in G_m$, measurement function $h(\mathbf{X}_k) \in G_m$, and measurement covariance noise $\mathcal{R}_k$ are constructed similarly to $\mathcal{H}_k$, but combined using diag instead of concatenation (e.g., $\mathcal{R}_k = \text{diag}(\sigma_{ori}^2, \sigma_{mp}^2)$).

$$\mathcal{H}_k = \frac{\partial}{\partial \epsilon}\left[\log\left(h(\hat{\boldsymbol{\mu}}_k^-)^{-1} h(\hat{\boldsymbol{\mu}}_k^- \exp([\epsilon]_G^\wedge))\right)\right]_{G_m}^\vee |_{\epsilon=0}$$
$$= \begin{cases} [\mathcal{H}_{ori}^T \quad \mathcal{H}_{mp/dist}^T]^T & \text{no FC} \\ [\mathcal{H}_{ori}^T \quad \mathcal{H}_{mp/dist}^T \quad \mathcal{H}_{ls,k}^T]^T & \text{left FC} \\ [\mathcal{H}_{ori}^T \quad \mathcal{H}_{mp/dist}^T \quad \mathcal{H}_{rs,k}^T]^T & \text{right FC} \\ [\mathcal{H}_{ori}^T \quad \mathcal{H}_{mp/dist}^T \quad \mathcal{H}_{ls,k}^T \quad \mathcal{H}_{rs,k}^T]^T & \text{both FC} \end{cases} \tag{29}$$

Orientation Update

The orientation update utilizes the orientation measurement to update the state estimate as defined by Eq. (30), with measurement noise variance σ_{ori}^2 (9×1 vector).

$$h_{ori}(\mathbf{X}_k) = \text{diag}(\boldsymbol{R}_k^p, \boldsymbol{R}_k^{ls}, \boldsymbol{R}_k^{rs}) \in SO(3)^3, \quad \mathbf{Z}_{ori} = \text{diag}(\breve{\boldsymbol{R}}_k^p, \breve{\boldsymbol{R}}_k^{ls}, \breve{\boldsymbol{R}}_k^{rs}) \tag{30}$$

$\mathcal{H}_{ori}$ along with other components of $\mathcal{H}_k$ are calculated by applying Eq. (29) to their corresponding measurement functions, followed by tedious algebraic manipulation and first order linearization (i.e., $\exp([\epsilon]^\wedge) \approx \mathbf{I} + [\epsilon]^\wedge$). The derivation for $\mathcal{H}_{ori}$ (Eq. (31)) can be solved trivially as $[\log(h_{ori}(\hat{\boldsymbol{\mu}}_k^-)^{-1} h_{ori}(\hat{\boldsymbol{\mu}}_k^- \exp([\epsilon]_G^\wedge)))]^\vee = [(\boldsymbol{\epsilon}_{\boldsymbol{\phi}}^p)^T \ (\boldsymbol{\epsilon}_{\boldsymbol{\phi}}^{ls})^T \ (\boldsymbol{\epsilon}_{\boldsymbol{\phi}}^{rs})^T]^T$, where $\boldsymbol{\epsilon}_{\mathbf{T}}^b = [(\boldsymbol{\epsilon}_{\boldsymbol{\rho}}^b)^T \ (\boldsymbol{\epsilon}_{\boldsymbol{\phi}}^b)^T]^T$ for body segment $b \in \{p, ls, rs\}$.

$$\mathcal{H}_{ori} = \left[\begin{array}{ccc|c} \mathbf{0}_{3\times3}\,\mathbf{I}_{3\times3} & & & \\ & \mathbf{0}_{3\times3}\,\mathbf{I}_{3\times3} & & \mathbf{0}_{9\times9} \\ & & \mathbf{0}_{3\times3}\,\mathbf{I}_{3\times3} & \end{array}\right] \tag{31}$$

Pelvis Height Assumption

The pelvis height assumption softly constrains the pelvis z position to be close to initial standing height z_p as defined by Eq. (32) (represented in vector space of its Lie algebra) and Eq. (33), with measurement noise variance σ_{mp}^2 (1×1 vector). This assumption is used only when inter-IMU distance measurement is not available. $\boldsymbol{i}_x, \boldsymbol{i}_y, \boldsymbol{i}_z$, and $\boldsymbol{i}_0$ denote 4×1 vectors whose 1^{st} to 4^{th} rows, respectively, are 1, while the rest are 0; they are used below to select rows, columns, or elements from matrices.

$$[\log(h_{mp}(\mathbf{X}_k))]^\vee = \boldsymbol{i}_z^T\, \boldsymbol{T}_k^p \boldsymbol{i}_0 = \begin{bmatrix} 0 & 0 & 1 & 0 \end{bmatrix} \begin{bmatrix} \boldsymbol{R}_k^p & \boldsymbol{p}_k^p \\ \mathbf{0}_{1\times3} & 1 \end{bmatrix} \begin{bmatrix} 0 \\ 0 \\ 0 \\ 1 \end{bmatrix} = \begin{bmatrix} 0 & 0 & 1 & 0 \end{bmatrix} \begin{bmatrix} \boldsymbol{p}_k^p \\ 1 \end{bmatrix} = p_{z,k}^p \in \mathbb{R} \tag{32}$$

$$[\log(\mathbf{Z}_{mp})]^\vee = z_p \in \mathbb{R} \tag{33}$$

The derivation of $\mathcal{H}_{mp,k} = \frac{\partial}{\partial \epsilon}[\log(h_{mp}(\hat{\boldsymbol{\mu}}_k^-)^{-1} h_{mp}(\hat{\boldsymbol{\mu}}_k^- \exp([\epsilon]_G^\wedge)))]^\vee|_{\epsilon=0}$ is shown in Eqs. (34)-(36). Taking best estimate $\mathbf{X}_k = \hat{\boldsymbol{\mu}}_k^-$ gives us Eq. (34).

$$[\log(h_{mp}(\hat{\boldsymbol{\mu}}_k^-))]^\vee = \boldsymbol{i}_z^T\, \hat{\boldsymbol{T}}_k^{p-} \boldsymbol{i}_0 \tag{34}$$

Preprints (www.preprints.org) | NOT PEER-REVIEWED | Posted: 3 November 2020 doi:10.20944/preprints202011.0166.v1

$$
\begin{aligned}
[\log(h_{mp}(\hat{\boldsymbol{\mu}}_k^- \exp([\epsilon]_G^\wedge)))]^\vee &= \boldsymbol{i}_z^T\, \hat{\boldsymbol{T}}_k^{p-} \exp([\boldsymbol{\epsilon}_{\mathbf{T}}^p]^\wedge)\boldsymbol{i}_0 \\
&\approx \boldsymbol{i}_z^T\, \hat{\boldsymbol{T}}_k^{p-}\boldsymbol{i}_0 + \boldsymbol{i}_z^T\, \hat{\boldsymbol{T}}_k^{p-}[\boldsymbol{\epsilon}_{\mathbf{T}}^p]^\wedge \boldsymbol{i}_0, \quad \text{1st order linearization} \\
&\text{Use Eq. (11), } [\boldsymbol{a}]^\wedge\, \boldsymbol{b} = [\boldsymbol{b}]^\odot\, \boldsymbol{a}, \text{ to bring } \boldsymbol{\epsilon}_{\mathbf{T}}^p \text{ to right of } \boldsymbol{i}_0 \\
&= [\log(h_{mp}(\hat{\boldsymbol{\mu}}_k^-))]^\vee + \boldsymbol{i}_z^T\, \hat{\boldsymbol{T}}_k^{p-}[\boldsymbol{i}_0]^\odot\, \boldsymbol{\epsilon}_{\mathbf{T}}^p
\end{aligned}
\tag{35}
$$

Remember $\boldsymbol{\epsilon}_{\mathbf{T}}^p$ is a subvector of $\boldsymbol{\epsilon}$ as defined in Sec. 3.1 and is the Lie algebra error of the state in its compact vector representation. Note that if measurement function $h_a(\mathbf{X}_k) \in$ Lie group $\mathbb{R}^b$, then $[\log(h_a(\hat{\boldsymbol{\mu}}_k^-)^{-1}h_a(\mathbf{X}_k))]^\vee = [\log(h_a(\mathbf{X}_k))]^\vee - [\log(h_a(\hat{\boldsymbol{\mu}}_k^-))]^\vee = [\log(h_a(\hat{\boldsymbol{\mu}}_k^- \exp([\epsilon]_G^\wedge)))]^\vee - [\log(h_a(\hat{\boldsymbol{\mu}}_k^-))]^\vee$ by applying Eqs. (15) and (13) (inverse of Lie group $\mathbb{R}^n$). Finally, $\mathcal{H}_{mp,k}$ is calculated as shown in Eq. (36).

$$
\begin{aligned}
\mathcal{H}_{mp,k} &= \tfrac{\partial}{\partial \boldsymbol{\epsilon}}[\log(h_{mp}(\hat{\boldsymbol{\mu}}_k^-)^{-1}h_{mp}(\hat{\boldsymbol{\mu}}_k^- \exp([\epsilon]_G^\wedge)))]^\vee|_{\boldsymbol{\epsilon}=0} \\
&= \tfrac{\partial}{\partial \boldsymbol{\epsilon}}\left([\log(h_{mp}(\hat{\boldsymbol{\mu}}_k^- \exp([\epsilon]_G^\wedge)))]^\vee - [\log(h_{mp}(\hat{\boldsymbol{\mu}}_k^-))]^\vee\right)|_{\boldsymbol{\epsilon}=0} \\
&= \Big[\underbrace{\boldsymbol{i}_z^T\, \hat{\boldsymbol{T}}_k^{p-}[\boldsymbol{i}_0]^\odot}_{1\times 6} \;\; \mathbf{0}_{1\times 6} \;\; \mathbf{0}_{1\times 6} \;\vdots\; \mathbf{0}_{1\times 9}\Big]
\end{aligned}
\tag{36}
$$

Zero Velocity Update and Flat Floor Assumption

When step is detected, the ankle velocity is enforced to be zero and the ankle z position is brought to near the floor level, z_f (i.e., flat floor assumptions). The corresponding measurement function is defined by Eq. (37), with measurement noise variance σ_{ls}^2 (4×1 vector).

$$
[\log(h_{ls}(\mathbf{X}_k))]^\vee = \begin{bmatrix} \boldsymbol{v}^{ls} \\ \boldsymbol{i}_z^T\, \boldsymbol{T}_k^{ls}\boldsymbol{i}_0 \end{bmatrix} = \begin{bmatrix} \boldsymbol{v}^{ls} \\ p_{z,k}^{ls} \end{bmatrix} \in \mathbb{R}^4, \quad [\log(\mathbf{Z}_{ls})]^\vee = \begin{bmatrix} \mathbf{0}_{3\times 1} \\ z_f \end{bmatrix}
\tag{37}
$$

The zero velocity part of $\mathcal{H}_{ls,k}$ (Eq. (38)) and $\mathcal{H}_{rs,k}$ can also be calculated trivially, while the flat floor assumption can be calculated similarly as $\mathcal{H}_{mp,k}$ but the z position set to floor height, z_f, instead of the pelvis standing height, z_p.

$$
\begin{aligned}
\mathcal{H}_{ls,k} &= \tfrac{\partial}{\partial \boldsymbol{\epsilon}}[\log(h_{ls}(\hat{\boldsymbol{\mu}}_k^-)^{-1}h_{ls}(\hat{\boldsymbol{\mu}}_k^- \exp([\epsilon]_G^\wedge)))]^\vee|_{\boldsymbol{\epsilon}=0} \\
&= \tfrac{\partial}{\partial \boldsymbol{\epsilon}}\left([\log(h_{ls}(\hat{\boldsymbol{\mu}}_k^- \exp([\epsilon]_G^\wedge)))]^\vee - [\log(h_{ls}(\hat{\boldsymbol{\mu}}_k^-))]^\vee\right)|_{\boldsymbol{\epsilon}=0} \\
&= \Bigg[\underbrace{\begin{matrix} \mathbf{0}_{3\times 6} & \mathbf{0}_{3\times 6} & \mathbf{0}_{3\times 6} \\ \mathbf{0}_{1\times 6} & \boldsymbol{i}_z^T\, \hat{\boldsymbol{T}}_k^{ls-}[\boldsymbol{i}_0]^\odot & \mathbf{0}_{1\times 6} \end{matrix}}_{\text{pose states in } SE(3)} \;\vdots\; \underbrace{\begin{matrix} \mathbf{0}_{3\times 3} & \mathbf{I}_{3\times 3} & \mathbf{0}_{3\times 3} \\ \mathbf{0}_{1\times 3} & \mathbf{0}_{1\times 3} & \mathbf{0}_{1\times 3} \end{matrix}}_{\text{velocity states}}\Bigg]
\end{aligned}
\tag{38}
$$

Left and Right Ankle Distance Measurement

When the inter-IMU distance between the ankles, $\breve{d}_k^{lra}$, is available, ankle distance measurement is incorporated as a soft distance constraint. The measurement function is defined by Eq. (40), with measurement noise variance σ_{lra}^2 (1×1 vector). $\tau_{lra}(\mathbf{X}_k)$ (Eq. (39)) is the vector that points from the right ankle to the left ankle, where ${}^{ls}\boldsymbol{p}^{la}$ is the position of the left ankle expressed in left shank frame, and ${}^{rs}\boldsymbol{p}^{ra}$ is the position of the right ankle expressed in right shank frame. We have chosen that the ankles are at the origin of their respective shank frames. Note that matrix $\mathbf{E}$ converts homogeneous 4×1 coordinates to standard 3×1 coordinates (i.e., drops the 1 from the end of the 4×1 vector).

$$
\tau_{lra}(\mathbf{X}_k) = \overbrace{\begin{bmatrix} \mathbf{I}_{3\times 3} & \mathbf{0}_{3\times 1} \end{bmatrix}}^{\mathbf{E}}(\overbrace{\boldsymbol{T}_k^{ls}\;{}^{ls}\boldsymbol{p}^{la}}^{\text{left ankle in } W} - \overbrace{\boldsymbol{T}_k^{rs}\;{}^{rs}\boldsymbol{p}^{ra}}^{\text{right ankle in } W}), \quad {}^{ls}\boldsymbol{p}^{la} = {}^{rs}\boldsymbol{p}^{ra} = \overbrace{\begin{bmatrix} 0 & 0 & 0 & 1 \end{bmatrix}^T}^{\text{origin of frame}}
\tag{39}
$$

By taking the squared Euclidean distance of $\tau_{lra}(\mathbf{X}_k)$ (i.e., $||\,\tau_{lra}(\mathbf{X}_k)||^2$), we can get the ankle distance measurement model.

$$[\log(h_{lra}(\mathbf{X}_k))]^\vee = (\tau_{lra}(\mathbf{X}_k))^T\,\tau_{lra}(\mathbf{X}_k) \in \mathbb{R}, \quad [\log(\mathbf{Z}_{lra})]^\vee = (\tilde{d}_k^{lra})^2 \tag{40}$$

To solve for $\mathcal{H}_{lra,k}$ (Eq. (44)), we first solved for $[\log(h_{lra}(\mathbf{X}_k))]^\vee$ at $\mathbf{X}_k = \hat{\boldsymbol{\mu}}_k^-$ (Eq. (41)).

$$\tau_{lra}(\hat{\boldsymbol{\mu}}_k^-) = \mathbf{E}(\hat{\mathbf{T}}_k^{ls-}\,{}^{ls}\boldsymbol{p}^{la} - \hat{\mathbf{T}}_k^{rs-}\,{}^{rs}\boldsymbol{p}^{ra}), \quad [\log(h_{lra}(\hat{\boldsymbol{\mu}}_k^-))]^\vee = (\tau_{lra}(\hat{\boldsymbol{\mu}}_k^-))^T\,\tau_{lra}(\hat{\boldsymbol{\mu}}_k^-) \tag{41}$$

Then solve for $\tau_{lra}(\hat{\boldsymbol{\mu}}_k^- \exp([\epsilon]_G^\wedge))$ and $[\log(h_{lra}(\hat{\boldsymbol{\mu}}_k^- \exp([\epsilon]_G^\wedge)))]^\vee$ as shown in Eqs. (42) and (43).

$$\begin{aligned}
\tau_{lra}(\hat{\boldsymbol{\mu}}_k^- \exp([\epsilon]_G^\wedge)) &= \mathbf{E}(\hat{\mathbf{T}}_k^{ls-}\exp([\boldsymbol{\epsilon}_{\mathbf{T}}^{ls}]^\wedge)\,{}^{ls}\boldsymbol{p}^{la} - \hat{\mathbf{T}}_k^{rs-}\exp([\boldsymbol{\epsilon}_{\mathbf{T}}^{rs}]^\wedge)\,{}^{rs}\boldsymbol{p}^{ra}) \\
&\quad \text{Take the 1st order approximation} \\
&\approx \mathbf{E}(\hat{\mathbf{T}}_k^{ls-}\,{}^{ls}\boldsymbol{p}^{la} - \hat{\mathbf{T}}_k^{rs-}\,{}^{rs}\boldsymbol{p}^{ra} + \hat{\mathbf{T}}_k^{ls-}[\boldsymbol{\epsilon}_{\mathbf{T}}^{ls}]^\wedge\,{}^{ls}\boldsymbol{p}^{la} - \hat{\mathbf{T}}_k^{rs-}[\boldsymbol{\epsilon}_{\mathbf{T}}^{rs}]^\wedge\,{}^{rs}\boldsymbol{p}^{ra}) \\
&= \tau_{lra}(\hat{\boldsymbol{\mu}}_k^-) + \overbrace{\mathbf{E}(\,\hat{\mathbf{T}}_k^{ls-}[{}^{ls}\boldsymbol{p}^{la}]^\odot\,\boldsymbol{\epsilon}_{\mathbf{T}}^{ls} - \hat{\mathbf{T}}_k^{rs-}[{}^{rs}\boldsymbol{p}^{ra}]^\odot\,\boldsymbol{\epsilon}_{\mathbf{T}}^{rs})}^{\boldsymbol{\Gamma}_{lra}}, \quad \text{Using Eq. (11)}
\end{aligned} \tag{42}$$

$$\begin{aligned}
[\log(h_{lra}(\hat{\boldsymbol{\mu}}_k^- \exp([\epsilon]_G^\wedge)))]^\vee &= \left(\tau_{lra}(\hat{\boldsymbol{\mu}}_k^-) + \boldsymbol{\Gamma}_{lra}\right)^T\left(\tau_{lra}(\hat{\boldsymbol{\mu}}_k^-) + \boldsymbol{\Gamma}_{lra}\right) \\
&\quad \text{Assume 2nd order error } \approx 0 \\
&= \tau_{lra}(\hat{\boldsymbol{\mu}}_k^-)^T\,\tau_{lra}(\hat{\boldsymbol{\mu}}_k^-) + 2\,\tau_{lra}(\hat{\boldsymbol{\mu}}_k^-)^T\boldsymbol{\Gamma}_{lra} + \cancelto{\approx 0}{\boldsymbol{\Gamma}_{lra}^T\boldsymbol{\Gamma}_{lra}} \\
&= [\log(h_{lra}(\hat{\boldsymbol{\mu}}_k^-))]^\vee \\
&\quad + 2\,\tau_{lra}(\hat{\boldsymbol{\mu}}_k^-)^T\mathbf{E}(\,\hat{\mathbf{T}}_k^{ls-}[{}^{ls}\boldsymbol{p}^{la}]^\odot\,\boldsymbol{\epsilon}_{\mathbf{T}}^{ls} - \hat{\mathbf{T}}_k^{rs-}[{}^{rs}\boldsymbol{p}^{ra}]^\odot\,\boldsymbol{\epsilon}_{\mathbf{T}}^{rs})
\end{aligned} \tag{43}$$

$$\begin{aligned}
\mathcal{H}_{lra,k} &= \tfrac{\partial}{\partial\epsilon}[\log(h_{lra}(\hat{\boldsymbol{\mu}}_k^-)^{-1}h_{lra}(\hat{\boldsymbol{\mu}}_k^- \exp([\epsilon]_G^\wedge)))]^\vee|_{\epsilon=0} \\
&= \tfrac{\partial}{\partial\epsilon}\left([\log(h_{lra}(\hat{\boldsymbol{\mu}}_k^- \exp([\epsilon]_G^\wedge)))]^\vee - [\log(h_{lra}(\hat{\boldsymbol{\mu}}_k^-))]^\vee\right)|_{\epsilon=0} \\
&= \tfrac{\partial}{\partial\epsilon}\left(2\,\tau^{lra}(\hat{\boldsymbol{\mu}}_k^-)^T\mathbf{E}(\,\hat{\mathbf{T}}_k^{ls-}[{}^{ls}\boldsymbol{p}^{la}]^\odot\,\boldsymbol{\epsilon}_{\mathbf{T}}^{ls} - \hat{\mathbf{T}}_k^{rs-}[{}^{rs}\boldsymbol{p}_0^{rs}]^\odot\,\boldsymbol{\epsilon}_{\mathbf{T}}^{rs})\right)|_{\epsilon=0} \\
&= \Big[\;\mathbf{0}_{1\times 6}\;\vdots\;\underbrace{2\,\tau_{lra}(\hat{\boldsymbol{\mu}}_k^-)^T\mathbf{E}\,\hat{\mathbf{T}}_k^{ls-}[{}^{ls}\boldsymbol{p}^{la}]^\odot}_{1\times 6}\;\vdots\;\underbrace{-2\,\tau_{lra}(\hat{\boldsymbol{\mu}}_k^-)^T\mathbf{E}\,\hat{\mathbf{T}}_k^{rs-}[{}^{rs}\boldsymbol{p}^{ra}]^\odot}_{1\times 6}\;\vdots\;\mathbf{0}_{1\times 9}\;\Big]
\end{aligned} \tag{44}$$

Pelvis-to-Ankle Distance Measurement

In addition to the soft ankle distance constraint, the ankle to pelvis vector is inferred from the ankle to pelvis distance measurements while assuming hinged knee joints and constant body segment lengths. The measurement function is defined by Eq. (45), with measurement noise variance σ^2_{pla} (3×1 vector), where ${}^{p}\boldsymbol{p}^{mp}$ is the position of the mid-pelvis expressed in pelvis frame, and ${}^{ls}\boldsymbol{p}^{la}$ is the position of the left ankle expressed in left shank frame. We have chosen that the mid-pelvis and ankle are at the origin of their corresponding reference frames.

$$[\log(h_{pla}(\mathbf{X}_k))]^\vee = \mathbf{E}(\overbrace{\mathbf{T}_k^{p}\,{}^{p}\boldsymbol{p}^{mp}}^{\text{mid-pelvis in } W} - \overbrace{\mathbf{T}_k^{ls}\,{}^{ls}\boldsymbol{p}^{la}}^{\text{left ankle in } W}) \in \mathbb{R}^3, \quad {}^{p}\boldsymbol{p}^{mp} = {}^{ls}\boldsymbol{p}^{la} = \begin{bmatrix}0 & 0 & 0 & 1\end{bmatrix}^T \tag{45}$$

The measurement pelvis to left ankle vector can be calculated from the measured pelvis to left ankle distance, $\tilde{d}_k^{pla}$ as shown in Eq. (46) which is the Lie Group reformulation of [26, Eq. 4]. In essence, Eq. (47) calculates the most probably knee angle assuming hinged knee joint and constant body segment lengths, then Eq. (46) adds the thigh (expressed in shank coordinate system with knee angle $\hat{\theta}_k^{lk}$) and shank long axis to the hips to obtain the pelvis-to-ankle vector. See Appendix A for derivation. There are two solutions for $\hat{\theta}_k^{lk}$ due to the inverse cosine in Eq. (47). We chose the $\hat{\theta}_k^{lk}$ value as that closer to the current left knee angle estimate from the prediction step. Note that this measurement function

Preprints (www.preprints.org) | NOT PEER-REVIEWED | Posted: 3 November 2020 doi:10.20944/preprints202011.0166.v1

could also be formulated as a linearized Euclidean distance between the pelvis and ankle (i.e., similar to Eq. 44); however, a preliminary exploration of this approach showed poorer performance.

$$[\log(\mathbf{Z}_{pla,k})]^{\vee} = \overbrace{\frac{d^p}{2}\,\hat{\mathbf{T}}_k^{p-}\;\boldsymbol{i}_y - d^{ls}\,\hat{\mathbf{T}}_k^{ls-}\;\boldsymbol{i}_z}^{\boldsymbol{\psi}_{pla}=\text{half pelvis } y\text{-axis + shank } z\text{-axis}} + \overbrace{d^{lt}\,\hat{\mathbf{T}}_k^{ls-}(\boldsymbol{i}_x \sin(\hat{\theta}_k^{lk}) - \boldsymbol{i}_z \cos(\hat{\theta}_k^{lk}))}^{\text{thigh } z\text{-axis in shank frame}} \in \mathbb{R}^3 \tag{46}$$

$$\hat{\theta}_k^{lk} = \cos^{-1}\left(\frac{\alpha\gamma \pm \beta\sqrt{\alpha^2+\beta^2-\gamma^2}}{\alpha^2+\beta^2}\right) \text{ where } \begin{array}{l} \alpha = -2d^{lt}\boldsymbol{\psi}_{pla}^T\,\hat{\mathbf{T}}_k^{ls-}\;\boldsymbol{i}_z, \quad \beta = 2d^{lt}\boldsymbol{\psi}_{pla}^T\,\hat{\mathbf{T}}_k^{ls-}\;\boldsymbol{i}_x, \\ \gamma = (\check{d}_k^{pla})^2 - \boldsymbol{\psi}_{pla}^T\boldsymbol{\psi}_{pla} - (d^{lt})^2 \end{array} \tag{47}$$

To calculate for $\mathcal{H}_{pla,k}$, we first solved for $[\log(h_{pla}(\mathbf{X}_k))]^{\vee}$ at $\mathbf{X}_k = \hat{\boldsymbol{\mu}}_k^-$ similar to Eq. (41).

$$[\log(h_{pla}(\hat{\boldsymbol{\mu}}_k^-))]^{\vee} = \tau_{pla}(\hat{\boldsymbol{\mu}}_k^-) = \mathbf{E}(\hat{\mathbf{T}}_k^{p-}\,{}^p\boldsymbol{p}^{mp} - \hat{\mathbf{T}}_k^{ls-}\,{}^{ls}\boldsymbol{p}^{la}) \tag{48}$$

Then solve for $[\log(h_{pla}(\hat{\boldsymbol{\mu}}_k^- \exp([\epsilon]_G^{\wedge})))]^{\vee}$ similar to Eq. (42) (i.e., distance between mid-pelvis and left ankle) giving us $[\log(h_{pla}(\hat{\boldsymbol{\mu}}_k^- \exp([\epsilon]_G^{\wedge})))]^{\vee} = \tau_{pla}(\hat{\boldsymbol{\mu}}_k^-) + \boldsymbol{\Gamma}_{pla}$. $\mathcal{H}_{pla,k}$ is then calculated as shown in Eq. (49). The right side of the pelvis-to-ankle distance measurement (i.e., $h_{pra}(\hat{\boldsymbol{\mu}}_k^-)$, $\mathbf{Z}_{pra}$, $\mathcal{H}_{pra,k}$) can be solved similarly to the left side.

$$\begin{aligned}
\mathcal{H}_{pla,k} &= \tfrac{\partial}{\partial\epsilon}[\log(h_{pla}(\hat{\boldsymbol{\mu}}_k^-)^{-1}h_{pla}(\hat{\boldsymbol{\mu}}_k^- \exp([\epsilon]_G^{\wedge})))]^{\vee}|_{\epsilon=0} \\
&= \tfrac{\partial}{\partial\epsilon}\left([\log(h_{pla}(\hat{\boldsymbol{\mu}}_k^- \exp([\epsilon]_G^{\wedge})))]^{\vee} - [\log(h_{pla}(\hat{\boldsymbol{\mu}}_k^-))]^{\vee}\right)|_{\epsilon=0} \\
&= \tfrac{\partial}{\partial\epsilon}\left(\tau_{pla}(\hat{\boldsymbol{\mu}}_k^-) + \boldsymbol{\Gamma}_{pla} - \tau_{pla}(\hat{\boldsymbol{\mu}}_k^-)\right)|_{\epsilon=0} \\
&= \tfrac{\partial}{\partial\epsilon}\left(\boldsymbol{\Gamma}_{pla}\right)|_{\epsilon=0} = \tfrac{\partial}{\partial\epsilon}\left(\mathbf{E}(\,\hat{\mathbf{T}}_k^{p-}[{}^p\boldsymbol{p}^{mp}]^{\odot}\,\epsilon_{\mathbf{T}}^{p} - \hat{\mathbf{T}}_k^{ls-}[{}^{ls}\boldsymbol{p}^{la}]^{\odot}\,\epsilon_{\mathbf{T}}^{ls})\right)|_{\epsilon=0} \\
&= \Big[\,\underbrace{\mathbf{E}\,\hat{\mathbf{T}}_k^{p-}[{}^p\boldsymbol{p}^{mp}]^{\odot}}_{1\times 6} \;\vdots\; \underbrace{-\mathbf{E}\,\hat{\mathbf{T}}_k^{ls-}[{}^{ls}\boldsymbol{p}^{la}]^{\odot}}_{1\times 6} \;\vdots\; \mathbf{0}_{1\times 6} \;\vdots\; \mathbf{0}_{1\times 9}\,\Big]
\end{aligned} \tag{49}$$

Covariance Limiter

Lastly, the error covariance of the position estimates of the three instrumented body segments must be prevented from growing unbounded and/or becoming badly conditioned, as will occur naturally when tracking global position of objects without any global position reference. At this step, a pseudo-measurement equal to the current state $\hat{\boldsymbol{\mu}}_k^+$ is used (implemented by Eq. (50)) with some measurement noise of variance σ_{lim} (9×1 vector). The covariance $\mathbf{P}_k^+$ is then calculated through Eqs. (51)-(53).

$$\mathcal{H}_{lim} = \begin{bmatrix} \overbrace{\mathbf{I}_{3\times3}}^{\text{mp pos.}}\;\mathbf{0}_{3\times3} & & & \mathbf{0}_{9\times9} \\ & \overbrace{\mathbf{I}_{3\times3}}^{\text{la pos.}}\;\mathbf{0}_{3\times3} & & \\ & & \overbrace{\mathbf{I}_{3\times3}}^{\text{ra pos.}}\;\mathbf{0}_{3\times3} & \end{bmatrix} \tag{50}$$

$$\mathcal{H}_k' = [\mathcal{H}_k^T \quad \mathcal{H}_{lim}^T]^T, \quad \mathcal{R}_k' = \text{diag}(\sigma_k^2, \sigma_{lim}^2) \tag{51}$$

$$\mathbf{K}_k' = \mathbf{P}_k^- \mathcal{H}_k'^T (\mathcal{H}_k' \mathbf{P}_k^- \mathcal{H}_k'^T + \mathcal{R}')^{-1} \tag{52}$$

$$\mathbf{P}_k^+ = \Phi_G(\boldsymbol{\nu}_k)(\mathbf{I} - \mathbf{K}_k'\mathcal{H}_k')\mathbf{P}_k^-\Phi_G(\boldsymbol{\nu}_k)^T \tag{53}$$

3.2.3. Satisfying Biomechanical Constraints

After the preceding updates, the joint positions or angles may be beyond their allowed range (i.e., knee hyperflexion). The constraint update corrects the kinematic state estimates to satisfy the biomechanical constraints of the human body by projecting the current *a posteriori* state estimate $\hat{\boldsymbol{\mu}}_k^+$ onto the constraint surface, guided by our uncertainty in each state variable, which is encoded by $\mathbf{P}_k^+$. The following biomechanical constraint equations are enforced: (i) estimated thigh long axis vector lengths equal the thigh lengths; (ii) both knees act as hinge joints (formulation similar to [11, Sec. 2.3 Eqs. (4)]); and (iii) the knee joint angle is within realistic range. The constraint functions are similar to [9, Sec. II-E.3] but expressed under $SE(3)$ state variables. The constrained state $\tilde{\boldsymbol{\mu}}_k^+$ can be calculated using the equations below, similar to the measurement update of [31] with zero noise, where $\mathcal{C}_k = [\mathcal{C}_{L,k}^T \quad \mathcal{C}_{R,k}^T]^T$. $\mathcal{C}_{L,k}$ is the concatenation of $\mathcal{C}_{ltl,k}$, $\mathcal{C}_{lkh,k}$, and $\mathcal{C}_{lkr,k}$; the last matrix is not concatenated when the knee angle, α_{lk}, is within its allowed range (i.e., $\alpha_{lk,min} \leq \alpha_{lk} \leq \alpha_{lk,max}$). $\mathcal{C}_{ltl,k}$, $\mathcal{C}_{lkh,k}$, and $\mathcal{C}_{lkr,k}$ corresponds to the biomechanical constraint for the left thigh length (ltl), left knee hinged joint (lkh), and left knee angle ROM (lkr), respectively, which will be described more later. $\mathcal{C}_{R,k}$ can be derived similarly, while $\mathbf{D}_k$ and $c(\hat{\boldsymbol{\mu}}_k^+))$ are constructed similarly to $\mathbf{Z}_k$.

$$\tilde{\boldsymbol{\mu}}_k^+ = \hat{\boldsymbol{\mu}}_k^+ \exp([\boldsymbol{\nu}_k]_G^\wedge) \tag{54}$$
$$\boldsymbol{\nu}_k = \mathbf{K}_k([\log(c(\hat{\boldsymbol{\mu}}_k^+)^{-1}\mathbf{D}_k)]_{G_c}^\vee \tag{55}$$
$$\mathbf{K}_k = \mathbf{P}_k^+ \mathcal{C}_k^T (\mathcal{C}_k \mathbf{P}_k^+ \mathcal{C}_k^T)^{-1}) \tag{56}$$
$$\mathcal{C}_k = \frac{\partial}{\partial \boldsymbol{\epsilon}}[\log(c(\hat{\boldsymbol{\mu}}_k^+)^{-1} c(\hat{\boldsymbol{\mu}}_k^+ \exp([\boldsymbol{\epsilon}]_G^\wedge)))]_{G_c}^\vee|_{\boldsymbol{\epsilon}=0} \tag{57}$$

Thigh Length Constraint

Firstly, the thigh length constraint is shown in Eq. (59), where $\tau_z^{lt}(\mathbf{X}_k)$ (Eq. (58)) denotes the thigh long axis vector and d^{lt} denotes the measured thigh length during calibration. ${}^p\boldsymbol{p}^{lh}$ is the position of the left hip expressed in pelvis frame, and ${}^{ls}\boldsymbol{p}^{lk}$ is the position of the left knee expressed in left shank frame. We have chosen that the left hip to be $\frac{d^p}{2}$ to the left of the mid-pelvis origin, and the left knee to be d^{ls} from the left shank origin (i.e., from the left ankle).

$$\tau_z^{lt}(\mathbf{X}_k) = \mathbf{E}(\overbrace{\boldsymbol{T}^p\ {}^p\boldsymbol{p}^{lh}}^{\text{hip jt. pos. in } W} - \overbrace{\boldsymbol{T}^{ls}\ {}^{ls}\boldsymbol{p}^{lk}}^{\text{knee jt. pos. in } W}), \quad {}^p\boldsymbol{p}^{lh} = \begin{bmatrix}0 & \frac{d^p}{2} & 0 & 1\end{bmatrix}^T, \quad {}^{ls}\boldsymbol{p}^{lk} = \begin{bmatrix}0 & 0 & d^{ls} & 1\end{bmatrix}^T \tag{58}$$
$$[\log(c_{ltl}(\mathbf{X}_k))]^\vee = (\tau_z^{lt}(\mathbf{X}_k))^T\, \tau_z^{lt}(\mathbf{X}_k) \in \mathbb{R}, \quad [\log(\mathbf{D}_{ltl})]^\vee = (d^{lt})^2 \tag{59}$$

$\mathcal{C}_{ltl,k}$ is calculated using Eq. (60).

$$\begin{aligned}\mathcal{C}_{ltl,k} &= \frac{\partial}{\partial \boldsymbol{\epsilon}}[\log(c_{ltl}(\hat{\boldsymbol{\mu}}_k^+)^{-1} c_{ltl}(\hat{\boldsymbol{\mu}}_k^+ \exp([\boldsymbol{\epsilon}]_G^\wedge)))]^\vee|_{\boldsymbol{\epsilon}=0} \\ &= \frac{\partial}{\partial \boldsymbol{\epsilon}}\left([\log(c_{ltl}(\hat{\boldsymbol{\mu}}_k^+ \exp([\boldsymbol{\epsilon}]_G^\wedge)))]^\vee - [\log(c_{ltl}(\hat{\boldsymbol{\mu}}_k^+))]^\vee\right)|_{\boldsymbol{\epsilon}=0}\end{aligned} \tag{60}$$

Following similar procedure to $\mathcal{H}_{lra,k}$, we obtain $\tau_z^{lt}(\hat{\boldsymbol{\mu}}_k^+ \exp([\boldsymbol{\epsilon}]_G^\wedge)) = \tau_z^{lt}(\hat{\boldsymbol{\mu}}_k^+) + \boldsymbol{\Gamma}_{ltz}$ (similar to Eq. (42)), and $[\log(c_{ltl}(\hat{\boldsymbol{\mu}}_k^+ \exp([\boldsymbol{\epsilon}]_G^\wedge)))]^\vee = [\log(c_{ltl}(\hat{\boldsymbol{\mu}}_k^+))]^\vee + 2(\tau_z^{lt}(\hat{\boldsymbol{\mu}}_k^+))^T \mathbf{E}(\hat{\mathbf{T}}_k^{p+}[{}^p\boldsymbol{p}^{lh}]^\odot\, \boldsymbol{\epsilon}_{\mathbf{T}}^p - \hat{\mathbf{T}}_k^{ls+}[{}^{ls}\boldsymbol{p}^{lk}]^\odot\, \boldsymbol{\epsilon}_{\mathbf{T}}^{ls})$ (similar to Eq. (43)), which if we substitute in Eq. (60) gives us Eq. (61)

$$\begin{aligned}\mathcal{C}_{ltl,k} &= \frac{\partial}{\partial \boldsymbol{\epsilon}}\left(2\,\tau_z^{lt}(\hat{\boldsymbol{\mu}}_k^+)^T \mathbf{E}(\hat{\mathbf{T}}_k^{p+}[{}^p\boldsymbol{p}^{lh}]^\odot\, \boldsymbol{\epsilon}_{\mathbf{T}}^p - \hat{\mathbf{T}}_k^{ls+}[{}^{ls}\boldsymbol{p}^{lk}]^\odot\, \boldsymbol{\epsilon}_{\mathbf{T}}^{ls})\right)|_{\boldsymbol{\epsilon}=0} \\ &= \Big[\underbrace{2(\tau_z^{lt}(\hat{\boldsymbol{\mu}}_k^+))^T \mathbf{E}\,\hat{\mathbf{T}}_k^{p+}[{}^p\boldsymbol{p}^{lh}]^\odot}_{1\times 6} \;\vdots\; \underbrace{-2(\tau_z^{lt}(\hat{\boldsymbol{\mu}}_k^+))^T \mathbf{E}\,\hat{\mathbf{T}}_k^{ls+}[{}^{ls}\boldsymbol{p}^{lk}]^\odot}_{1\times 6} \;\vdots\; \mathbf{0}_{1\times 6} \;\vdots\; \mathbf{0}_{1\times 9}\Big]\end{aligned} \tag{61}$$

Hinge Knee Joint Constraint

Secondly, the hinge knee joint constraint as defined by Eq. (62) is enforced by having the long (z) axis of the thigh to be perpendicular to the mediolateral axis (y) of the shank. For example, on the left leg, we would want $\boldsymbol{r}_y^{ls}$ be perpendicular to the thigh long axis vector $\tau_z^{lt}(\hat{\boldsymbol{\mu}}_k^+)$ (i.e., the dot product of $\boldsymbol{r}_y^{ls}$ and $\tau_z^{lt}(\hat{\boldsymbol{\mu}}_k^+)$ should be 0). Refer to Fig. 2 for visualization. This formulation is similar to [11, Sec. 2.3 Eqs. (4)].

$$[\log(c_{lkh}(\mathbf{X}_k))]^\vee = (\mathbf{E}\,\boldsymbol{T}^{ls}\boldsymbol{i}_y)^T\, \tau_z^{lt}(\mathbf{X}_k) = (\boldsymbol{r}_y^{ls})^T\, \tau_z^{lt}(\mathbf{X}_k) \in \mathbb{R}, \quad [\log(\mathbf{D}_{lkh})]^\vee = 0 \tag{62}$$

Following similar procedure to $\mathcal{C}_{ltl,k}$ and taking $\mathbf{X}_k = \hat{\boldsymbol{\mu}}_k^+$, $[\log(c_{lkh}(\hat{\boldsymbol{\mu}}_k^+))]^\vee$ and $[\log(c_{lkh}(\hat{\boldsymbol{\mu}}_k^+ \exp([\epsilon]_G^\wedge)))]^\vee$ can be calculated as shown in Eqs. (63) and (64), respectively.

$$[\log(c_{lkh}(\hat{\boldsymbol{\mu}}_k^+))]^\vee = (\mathbf{E}\,\hat{\mathbf{T}}^{ls+}\boldsymbol{i}_y)^T\,\tau_z^{lt}(\hat{\boldsymbol{\mu}}_k^+) \tag{63}$$

$$\begin{aligned}
[\log(c_{lkh}(\hat{\boldsymbol{\mu}}_k^+ \exp([\epsilon]_G^\wedge)))]^\vee &= (\mathbf{E}\,\hat{\mathbf{T}}^{ls+}\exp([\boldsymbol{\epsilon}_{\mathbf{T}}^{ls}]^\wedge)\boldsymbol{i}_y)^T(\tau_z^{lt}(\hat{\boldsymbol{\mu}}_k^+) + \boldsymbol{\Gamma}_{ltz}) \\
&\text{Taking 1st order approximation of exp} \\
&\approx (\mathbf{E}(\hat{\mathbf{T}}^{ls+} + \hat{\mathbf{T}}^{ls+}[\boldsymbol{\epsilon}_{\mathbf{T}}^{ls}]^\wedge)\boldsymbol{i}_y)^T(\tau_z^{lt}(\hat{\boldsymbol{\mu}}_k^+) + \boldsymbol{\Gamma}_{ltz}) \\
&\text{Assume 2nd order error } \approx 0 \\
&= (\mathbf{E}\,\hat{\mathbf{T}}^{ls+}\boldsymbol{i}_y)^T\,\tau_z^{lt}(\hat{\boldsymbol{\mu}}_k^+) + (\mathbf{E}\,\hat{\mathbf{T}}^{ls+}\,\boldsymbol{i}_y)^T\boldsymbol{\Gamma}_{ltz} \\
&\quad + (\tau_z^{lt}(\hat{\boldsymbol{\mu}}_k^+))^T\mathbf{E}\,\hat{\mathbf{T}}^{ls+}[\boldsymbol{\epsilon}_{\mathbf{T}}^{ls}]^\wedge\boldsymbol{i}_y + \underbrace{(\mathbf{E}\,\hat{\mathbf{T}}^{ls+}[\boldsymbol{\epsilon}_{\mathbf{T}}^{ls}]^\wedge\boldsymbol{i}_y)^T\boldsymbol{\Gamma}_{ltz}}_{\approx 0} \\
&= [\log(c_{lkh}(\hat{\boldsymbol{\mu}}_k^+))]^\vee + (\mathbf{E}\,\hat{\mathbf{T}}^{ls+}\,\boldsymbol{i}_y)^T\mathbf{E}(\,\hat{\mathbf{T}}_k^{p+}[{}^p\boldsymbol{p}^{lh}]^\odot\,\boldsymbol{\epsilon}_{\mathbf{T}}^p - \hat{\mathbf{T}}_k^{ls+}[{}^{ls}\boldsymbol{p}^{lk}]^\odot\,\boldsymbol{\epsilon}_{\mathbf{T}}^{ls}) \\
&\quad + (\tau_z^{lt}(\hat{\boldsymbol{\mu}}_k^+))^T\mathbf{E}\,\hat{\mathbf{T}}^{ls+}[\boldsymbol{i}_y]^\odot\,\boldsymbol{\epsilon}_{\mathbf{T}}^{ls}, \text{ by expanding } \boldsymbol{\Gamma}_{ltz} \text{ and using Eq. (11)}
\end{aligned} \tag{64}$$

$\mathcal{C}_{lkh,k}$ can be calculated using Eq. (65).

$$\begin{aligned}
\mathcal{C}_{lkh,k} &= \tfrac{\partial}{\partial\epsilon}[\log(c_{lkh}(\hat{\boldsymbol{\mu}}_k^+)^{-1}c_{lkh}(\hat{\boldsymbol{\mu}}_k^+\exp([\epsilon]_G^\wedge)))]^\vee|_{\epsilon=0} \\
&= \tfrac{\partial}{\partial\epsilon}\left([\log(c_{lkh}(\hat{\boldsymbol{\mu}}_k^+\exp([\epsilon]_G^\wedge)))]^\vee - [\log(c_{lkh}(\hat{\boldsymbol{\mu}}_k^+))]^\vee\right)|_{\epsilon=0}
\end{aligned} \tag{65}$$

Substituting Eqs. (63) and (64) into Eq. (65) gives us Eq. (66).

$$\mathcal{C}_{lkh,k} = \Big[\,\underbrace{(\mathbf{E}\,\hat{\mathbf{T}}^{ls+}\boldsymbol{i}_y)^T\mathbf{E}\,\hat{\mathbf{T}}^{p+}[{}^p\boldsymbol{p}^{lh}]^\odot}_{1\times 6},\ \underbrace{-(\mathbf{E}\,\hat{\mathbf{T}}^{ls+}\boldsymbol{i}_y)^T\mathbf{E}\,\hat{\mathbf{T}}^{ls+}[{}^{ls}\boldsymbol{p}^{lk}]^\odot + (\tau_z^{lt}(\hat{\boldsymbol{\mu}}_k^+))^T\mathbf{E}\,\hat{\mathbf{T}}^{ls+}[\boldsymbol{i}_y]^\odot}_{1\times 6},\ \mathbf{0}_{1\times 15}\,\Big] \tag{66}$$

Knee Range of Motion Constraint

Thirdly, the knee ROM constraint is defined by Eq. (69) and is only enforced if the knee angle, α_{lk}, is outside the allowed ROM. The bounded knee angle, α'_{lk}, is calculated by Eq. (67). Eq. (69) is obtained by expanding Eq. (67) to Eq. (68) which when rearranged gives us $[\log(c_{lkr}(\mathbf{X}_k))]^\vee$ (i.e., Lie group representation of [9, Eq. (26)]). Note that ${}^{ls}\boldsymbol{r}_z^{lt}$ is the normalized thigh long axis expressed in the left shank frame.

$$\alpha_{lk} = \tan^{-1}\left(\frac{-(\boldsymbol{r}_z^{ls})^T\,\boldsymbol{r}_z^{lt}}{-(\boldsymbol{r}_x^{ls})^T\,\boldsymbol{r}_z^{lt}}\right) + \frac{\pi}{2}, \quad \alpha'_{lk} = \mathbf{min}(\alpha_{lk,max}, \mathbf{max}(\alpha_{lk,min}, \alpha_{lk})) \tag{67}$$

$$\frac{-\,\boldsymbol{r}_z^{lt}\cdot\boldsymbol{r}_z^{ls}}{-\,\boldsymbol{r}_z^{lt}\cdot\boldsymbol{r}_x^{ls}} = \frac{\sin(\alpha'_{lk} - \frac{\pi}{2})}{\cos(\alpha'_{lk} - \frac{\pi}{2})} \tag{68}$$

$$[\log(c_{lkr}(\mathbf{X}_k))]^\vee = (\mathbf{E}\,\boldsymbol{T}^{ls}\overbrace{(\boldsymbol{i}_z\cos(\alpha'_{lk} - \tfrac{\pi}{2}) - \boldsymbol{i}_x\sin(\alpha'_{lk} - \tfrac{\pi}{2}))}^{{}^{ls}\boldsymbol{r}_z^{lt} = \text{long axis of left thigh in shank frame}})^T\,\tau_z^{lt}(\mathbf{X}_k) \in \mathbb{R}, \quad [\log(\mathbf{D}_{lkr})]^\vee = 0 \tag{69}$$

Following a similar procedure to $\mathcal{C}_{lkh,k}$ (i.e., replace $\boldsymbol{i}_y$ in Eq. (64) with ${}^{ls}\boldsymbol{r}_z^{lt}$) and taking $\mathbf{X}_k = \hat{\boldsymbol{\mu}}_k^+$, $\mathcal{C}_{lkr,k}$ can be calculated from $c_{lkr}(\hat{\boldsymbol{\mu}}_k^+\exp([\epsilon]_G^\wedge)) = [\log(c_{lkr}(\hat{\boldsymbol{\mu}}_k^+))]^\vee + (\mathbf{E}\,\hat{\mathbf{T}}^{ls+}\,{}^{ls}\boldsymbol{r}_z^{lt})^T\mathbf{E}(\,\hat{\mathbf{T}}_k^{p+}[{}^p\boldsymbol{p}^{lh}]^\odot\,\boldsymbol{\epsilon}_{\mathbf{T}}^p - \hat{\mathbf{T}}_k^{ls+}[{}^{ls}\boldsymbol{p}^{lk}]^\odot\,\boldsymbol{\epsilon}_{\mathbf{T}}^{ls}) + (\tau_z^{lt}(\hat{\boldsymbol{\mu}}_k^+))^T\mathbf{E}\,\hat{\mathbf{T}}^{ls+}[{}^{ls}\boldsymbol{r}_z^{lt}]^\odot\,\boldsymbol{\epsilon}_{\mathbf{T}}^{ls}$, as shown in Eq. (70).

$$\begin{aligned}
\mathcal{C}_{lkr,k} &= \tfrac{\partial}{\partial\epsilon}[\log(c_{lkr}(\hat{\boldsymbol{\mu}}_k^+)^{-1}c_{lkr}(\hat{\boldsymbol{\mu}}_k^+\exp([\epsilon]_G^\wedge)))]^\vee|_{\epsilon=0} \\
&= \tfrac{\partial}{\partial\epsilon}\left([\log(c_{lkr}(\hat{\boldsymbol{\mu}}_k^+\exp([\epsilon]_G^\wedge)))]^\vee - [\log(c_{lkr}(\hat{\boldsymbol{\mu}}_k^+))]^\vee\right)|_{\epsilon=0} \\
&= \Big[\,\underbrace{(\mathbf{E}\,\hat{\mathbf{T}}^{ls+}\,{}^{ls}\boldsymbol{r}_z^{lt})^T\mathbf{E}\,\hat{\mathbf{T}}^{p+}[{}^p\boldsymbol{p}^{lh}]^\odot}_{1\times 6},\ \underbrace{-(\mathbf{E}\,\hat{\mathbf{T}}^{ls+}\,{}^{ls}\boldsymbol{r}_z^{lt})^T\mathbf{E}\,\hat{\mathbf{T}}^{ls+}[{}^{ls}\boldsymbol{p}^{lk}]^\odot + (\tau_z^{lt}(\hat{\boldsymbol{\mu}}_k^+))^T\mathbf{E}\,\hat{\mathbf{T}}^{ls+}[{}^{ls}\boldsymbol{r}_z^{lt}]^\odot}_{1\times 6},\ \mathbf{0}_{1\times 15}\,\Big]
\end{aligned} \tag{70}$$

Preprints (www.preprints.org) | NOT PEER-REVIEWED | Posted: 3 November 2020 doi:10.20944/preprints202011.0166.v1

3.3. Post-Processing

The orientation of the pelvis and shanks are obtained from the state $\tilde{\boldsymbol{\mu}}_k^+$. The orientation of the left thigh, $\tilde{\boldsymbol{R}}^{lt+}$, can be calculated using $\tilde{\boldsymbol{R}}^{lt+} = [\, \tilde{\boldsymbol{r}}_y^{ls+} \times \tilde{\boldsymbol{r}}_z^{lt+} \,\vdots\, \tilde{\boldsymbol{r}}_y^{ls+} \,\vdots\, \tilde{\boldsymbol{r}}_z^{lt+} \,] = [\, [\mathbf{E}\, \tilde{\boldsymbol{T}}_k^{ls+}\, \boldsymbol{i}_y]^{\wedge}_{SO(3)}\, \tilde{\boldsymbol{r}}_z^{lt+} \,\vdots\, (\mathbf{E}\, \tilde{\boldsymbol{T}}_k^{ls+}\, \boldsymbol{i}_y) \,\vdots\, \tilde{\boldsymbol{r}}_z^{lt+} \,]$, where $\tilde{\boldsymbol{r}}_z^{lt+} = \tau_z^{lt}(\tilde{\boldsymbol{\mu}}_k^+)/||\, \tau_z^{lt}(\tilde{\boldsymbol{\mu}}_k^+)||$. The orientation of the right thigh, $\tilde{\boldsymbol{R}}^{rt+}$, is calculated similarly.

4. Experiment

An extension of the dataset from [9] was used to evaluate our *L5S* based algorithms. It involved movements listed in Table 1 (including dynamic movements) from nine healthy subjects (7 men and 2 women, weight 63.0 ± 6.8 kg, height 1.70 ± 0.06 m, age 24.6 ± 3.9 years old), with no known gait abnormalities. Raw data were captured using a commercial IMC (i.e., Xsens Awinda) with IMUs attached to the pelvis and ankles, compared against a benchmark OMC (i.e., Vicon Plug-in Gait) within an $\sim 4 \times 4$ m^2 capture area. The experiment was approved by the Human Research Ethics Board of the University of New South Wales (UNSW) with approval number HC180413.

Table 1. Types of movements done in the validation experiment.

Movement	Description	Duration	Group
Walk	Walk straight and return	$\sim$ 30 s	F
Figure-of-eight	Walk along figure-of-eight path	$\sim$ 60 s	F
Zig-zag	Walk along zig-zag path	$\sim$ 60 s	F
5-minute walk	Unscripted walk and stand	$\sim$ 300 s	F
Speedskater	Speedskater on the spot	$\sim$ 30 s	D
TUG	Timed up-and-go test	$\sim$ 30 s	D
Jog	Jog straight and return	$\sim$ 30 s	D
Jumping jacks	Jumping jacks on the spot	$\sim$ 30 s	D
High-knee jog	High-knee jog on the spot	$\sim$ 30 s	D

F denotes free walk, D denotes dynamic movements

Frame alignment and yaw offset calibrations are similar to [9, Sec. III-B]. The algorithm and calculations were implemented using Matlab 2020a. The initial position, orientation, and velocity ($\tilde{\boldsymbol{\mu}}_0^+$) were obtained from the Vicon benchmark system. $\mathbf{P}_0^+$ was set to $0.5\mathbf{I}_{27\times 27}$. The variance parameters used to generate the process and measurement error covariance matrix $\mathcal{Q}$ and $\mathcal{R}$ are shown in Table 2.

Table 2. Parameters for error covariance matrices, $\mathcal{Q}$ and $\mathcal{R}$.

$\mathcal{Q}$ Parameters		$\mathcal{R}$ Parameters					
σ_a^2 (m^2.s^{-4})	σ_ω^2 (rad^2.s^{-2})	σ_{ori}^2 (rad^2)	σ_{mp}^2 (m^2)	σ_{ls}^2 and σ_{rs}^2 (m^2.s^{-2} and m^2)	σ_{dl}^2 and σ_{dr}^2 (m^2)	σ_{da}^2 (m^2)	σ_{lim}^2 (m^2)
$10^2\mathbf{1}_9$	$10^3\mathbf{1}_9$	$1\mathbf{1}_9$	0.1	$[0.01\mathbf{1}_3 \quad 10^{-4}]$	10	1	$10\mathbf{1}_{18}$

where $\mathbf{1}_n$ is an $1 \times n$ row vector with all elements equal to 1.

The inter-IMU distance measurements, $\check{d}^{pla}$, $\check{d}^{pra}$, and $\check{d}^{lra}$, were simulated by calculating the distance from the mid-pelvis to the left and right ankles and adding normally distributed positional noise with different standard deviations (i.e., $\sigma_{dist} \in \{0, 0.01, \ldots, 0.1, 0.15, 0.2\}$ m). Each trial was simulated five times.

Lastly, the evaluation was done using the following metrics: (1) Mean position and orientation root-mean-square error (RMSE) (e.g., similar to [9,12] as shown in Eqs. (71) and (72)), where $\boldsymbol{p}_k^b$ and $\boldsymbol{R}_k^b$ are obtained from the benchmark OMC system, $\tilde{\boldsymbol{p}}_k^{b+}$ and $\tilde{\boldsymbol{R}}_k^{b+}$ are obtained from the algorithm. Note that as the global position of the estimate is still prone to drift due to the absence of an external global position reference, the root position of our system was set equal to that of the benchmark system (i.e., the mid-pelvis is placed at the origin in the world frame for all RMSE calculations). (2) joint angles RMSE with bias removed (i.e., the mean difference between the angles over each entire trial

Preprints (www.preprints.org) | NOT PEER-REVIEWED | Posted: 3 November 2020 doi:10.20944/preprints202011.0166.v1

was subtracted) and correlation coefficient (CC) of the hip in the sagittal (Y), frontal (X),and transverse (Z) planes and of the knee in the sagittal (Y) plane. Note that these joint angles are commonly used parameters in gait analysis. (3) Spatiotemporal gait parameters (e.g., total travelled distance (TTD) deviation, average stride length, and gait speed of the foot). Refer to [9, Sec. III] for more details.

$$e_{pos,k} = \frac{1}{N_{pos}} \sum_{b \in \mathbb{DP}} || \boldsymbol{p}_k^b - \tilde{\boldsymbol{p}}_k^{b+} ||, \quad N_{pos} = 6, \quad \mathbb{DP} = \{lh, rh, lk, rk, la, ra\} \tag{71}$$

$$e_{ori,k} = \frac{1}{N_{ori}} \sum_{b \in \mathbb{DO}} ||[\log(\boldsymbol{R}_k^b (\tilde{\boldsymbol{R}}_k^{b+})^T)]^\vee||, \quad N_{ori} = 2, \quad \mathbb{DO} = \{lt, rt\} \tag{72}$$

5. Results

5.1. Mean Position and Orientation RMSE, Joint Angle RMSE and CC

In this experiment, multiple variations of the algorithm were tested as shown in Table 3. Firstly, *L5S-3IMU* is the algorithm described in this paper (Sec. 3) with parameters listed in Table 2. The parameter for *L5S-3IMU* were selected by taking the best joint CC (i.e., mean of free walk and dynamic movements) from a grid search of parameters $\sigma_\omega^2 = \{1, 10, 10^2, 10^3\}$ rad^2/s^2 and $\sigma_{ori}^2 = \{10^{-2}, 10^{-1}, 1, 10\}$ rad^2. Secondly, *CKF-3IMU* and *CKF-3IMU+D* were the algorithms described in [9] and [26], respectively. Thirdly, *CKF-3I-KB* is a modified *CKF-3IMU* using similar parameters, measurement, and constraint functions as *L5S-3IMU*. The key difference between *CKF-3IMU* and *CKF-3I-KB* is that *CKF-3I-KB* allows knee bending, denoted by the suffix *KB*, during the constraint update. Fourthly, *L5S-3I-NO* is a variation of *L5S-3IMU* with $\sigma_\omega^2 = 10^7$ rad^2/s^2, $\sigma_{ori}^2 = 10^{-1}$ rad^2, and ${}^b\breve{\omega}_k = 0$ rad. The parameters were chosen to have high uncertainty on the tracked orientation (i.e., effectively not using the orientation measurements at all), leading to a variation of *L5S-3IMU* that is similar to our prior work *CKF-3IMU* which assumed orientation measurements were noise-free. Lastly, the black box output (i.e., pelvis, thigh, and shank orientations) from the MVN Studio software (denoted as *OSPS*), which illustrates the performance of a widely-accepted commercial wearable IMC system with an OSPS configuration. For the first to fourth variations, the $+D$ suffix means simulated inter-IMU distance measurements ($\sigma_{dist} = 0.1$ m) was used instead of the pelvis height assumption.

Table 3. The experiment was tested on the following algorithm variations.

Algorithm	Inter-IMU distance	Summary description
L5S-3IMU *L5S-3IMU+D*	N Y	Tracks position and orientation as described in Sec. 3 with parameters listed in Table 2.
CKF-3IMU [9] *CKF-3IMU+D* [26]	N Y	Only tracks position using a constrained KF.
CKF-3I-KB *CKF-3I-KB+D*	N Y	Modified *CKF-3IMU* using similar parameters as *L5S-3IMU* (Table 2). Also allows knee bending during the constraint update.
L5S-3I-NO *L5S-3I-NO+D*	N Y	*L5S-3IMU* with parameters that assume noise-free orientation (*NO*) measurements like *CKF-3IMU*.
OSPS	N	Output from a commercial OSPS wearable IMC system.

Fig. 4 shows the mean position and orientation RMSE, mean knee Y and hip joint angle RMSE (bias removed) and CC of different variations of *CKF-3IMU* and *L5S-3IMU* for both free walking and dynamic motions. Y, X, and Z refers to the sagittal, frontal, and transverse planes, respectively. *CKF-3IMU* performed well with free walking ($e_{pos} = 4.27$ cm, $e_{ori} = 15.85°$, $CC = 0.66$) [9]. However, a more extensive evaluation showed that it performed poorly for certain dynamic movements (e.g., high-knee jog with $e_{pos} = 18.15$ cm, $e_{ori} = 24.87°$, $CC = 0.02$). Removing the no-knee-bending assumption during the constraint update fixed this issue, as shown by the performance of *CKF-3I-KB* (e.g., high-knee jog improved by ~9 cm e_{pos}, ~9° e_{ori}, ~0.4 CC). *L5S-3I-NO* which is the *L5S* version of *CKF-3IMU* expectedly have similar performance with *CKF-3I-KB* (i.e., $\Delta e_{pos} < 0.5$ cm, $\Delta e_{ori} < 1°$, and

Preprints (www.preprints.org) | NOT PEER-REVIEWED | Posted: 3 November 2020 doi:10.20944/preprints202011.0166.v1

ΔCC 0.02 differences). *L5S-3IMU*, which tracked both position and orientation while assuming there is noise in the orientation measurements, had a slightly better performance (e.g., improved jumping jacks and high-knee jog by ~0.1 CC, $<$ 0.03 CC difference with other movement types). The use of simulated distance measurement with $\sigma_{dist} = 0.1$ m on *CKF-3I-KB*, *L5S-3I-NO*, and *L5S-3IMU* had slight effects for free walking, and a significant improvement for dynamic movements. For free walking, joint angle RMSE and CC of *L5S-3IMU+D* compared to *L5S-3IMU* improved by ~1° and $<$ 0.01 CC, while e_{pos} and e_{ori} slightly disimproved ($<$ 0.5 cm and $<$ 1°). The similar results suggest that inferring pelvis position from simulated distance measurement ($\sigma_{dist} = 0.1$ m) is comparable to our pelvis height assumption at least for free walking. For dynamic movements, the e_{pos}, e_{ori}, joint angle RMSE, and CC of *L5S-3IMU+D* improved by 2–16 cm, 0–40°, 1–9°, and $<$ 0.42, respectively; more significantly for movements TUG and high-knee jog.

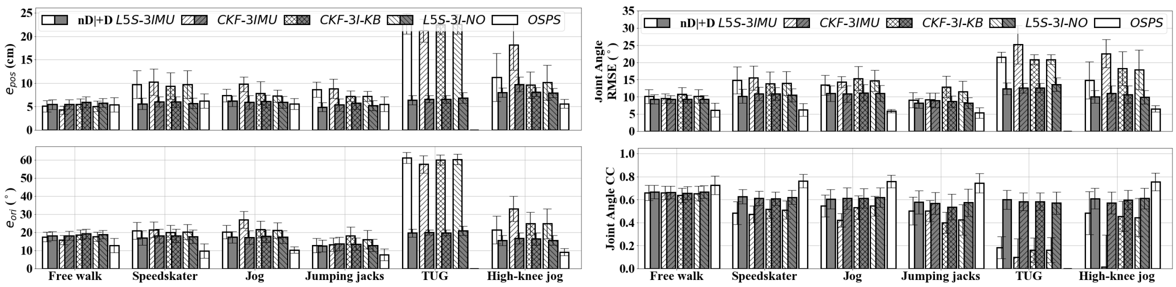

(a) Mean position and orientation RMSE **(b)** Joint angle RMSE and CC

Figure 4. The performance of *CKF*, *L5S*, and *OSPS* with and without using inter-IMU distance measurements at each motion type.

To give insight on how the accuracy of the simulated inter-IMU distance measurements affect pose estimation performance, Fig. 5 shows the mean of knee Y and hip joint angle RMSE and CC at different σ_{dist} values. At $\sigma_{dist} = 0.1$ m, the simulation showed comparable performance between *L5S-3IMU*, which implements pelvis height assumption, and *L5S-3IMU+D*, which implements inter-IMU distance measurement to supplement the pelvis position estimate, for free walking. Significant improvement for dynamic movements can be seen even for $\sigma_{dist} = 0.2$ m. These results suggest that the actual distance measurement sensor must have noise standard deviation $\sigma_{dist} \leq 0.1$ m to improve pose estimate performance. Note that the *+D* variation in Fig. 4 and in the experiments that follow were evaluated at $\sigma_{dist} = 0.1$ m.

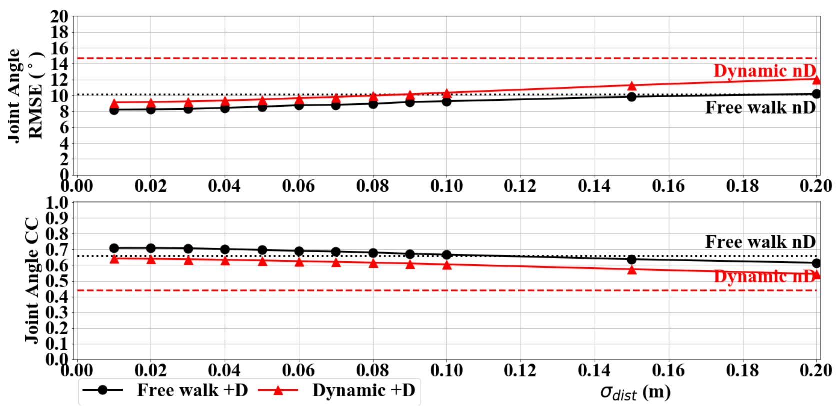

Figure 5. Joint angle RMSE (top) and CC (bottom) of free walk and dynamic movements at different noise level σ_{dist}. The broken lines represent *L5S-3IMU* results (denoted as *nD*) where inter-IMU distance measurements were not used. The solid lines represent *L5S-3IMU+D* results (denoted as *+D*) where we can observe slight and great improvements for free walk and dynamic movements, respectively.

5.2. Hip and Knee Joint Angle RMSE and CC

Fig. 4 shows the knee and hip joint angle RMSE (bias removed) and CC of *L5S-3IMU* and *L5S-3IMU+D* compared against the OMC output. Y, X, and Z refers to the sagittal, frontal, and transverse planes, respectively. Turning movements and half steps were manually removed from the per-step result of Walk movement and was denoted as Straight Walk. Note that sensor-to-body calibration was only done at the beginning of trial, not for each step. Between *L5S-3IMU* and *L5S-3IMU+D*, there was minimal hip and knee joint angle RMSE and CC improvement for free walking (~1° RMSE and ~0.03 CC difference). However, there was significant improvement for most dynamic movements, specifically, speed-skater, jog, high-knee jog, and TUG (e.g., $4-17°$ knee Y and hip Y joint angle RMSE improvements). Furthermore, the CC for dynamic movements started to reach similar performance with the free walk movement, indicating that inter-IMU distance measurements have indeed made the pose estimator capable of tracking more ADLs and not just walking.

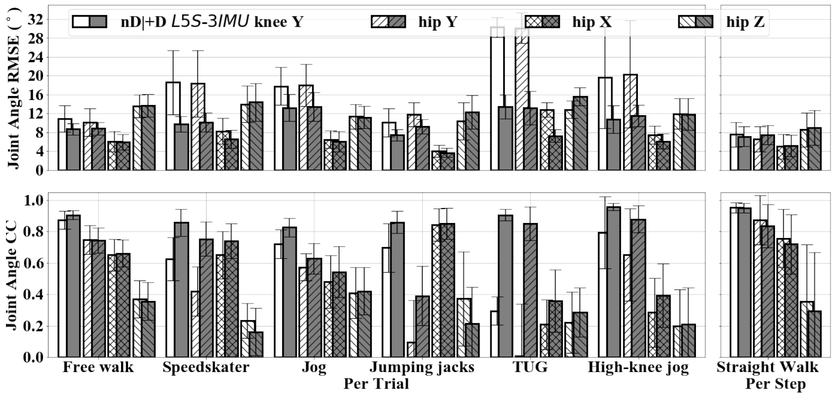

Figure 6. The CC of knee (Y) and hip (Y, X, Z) joint angles for *L5S-3IMU* (denoted as *nD*) and *L5S-3IMU+D* (denoted as *+D*) at each motion type.

Fig. 7 shows a sample Walk trial. At the peaks of knee Y angle, the distance between the pelvis and ankle positions of *L5S-3IMU+D* were a few cm shorter (i.e., pelvis position was lower than actual while ankle position was higher) than the actual distance resulting in higher knee Y angle peaks. Violations of our biomechanical constraints are also apparent at $t = 4$ to 5.5 s, where the subject makes a 180° turn. After the turn, *L5S-3IMU* and *L5S-3IMU+D* were able to recover during the straight walking ($t = 5.5$ to 9.74 s of Fig. 7). Notice that the bias between OSPS and OMC can be observed at $t = 0$ of the hip Y joint angle.

5.3. Spatiotemporal Gait Parameters

Table 4 shows the TTD, stride length, and gait speed accuracy computed from the global ankle position estimate of *L5S-3IMU*, *L5S-3IMU+D*, and the OMC system for free walk, jogging, and TUG. The use of inter-IMU distance measurements ($\sigma_{dist} = 0.1$ m) helped improve the TTD, stride length, and gait speed accuracy of free walk and TUG (e.g., TTD improved from ~9% to ~5%). Refer to the code repository for links to videos of sample trials.

6. Discussion

In this paper, a Lie group EKF algorithm for lower body pose estimation using only three IMUs, ergonomically placed on the ankles and sacrum to facilitate continuous recording outside the laboratory, was described and evaluated. The algorithm utilizes fewer sensors than other approaches reported in the literature, at the cost of reduced accuracy.

Preprints (www.preprints.org) | NOT PEER-REVIEWED | Posted: 3 November 2020 doi:10.20944/preprints202011.0166.v1

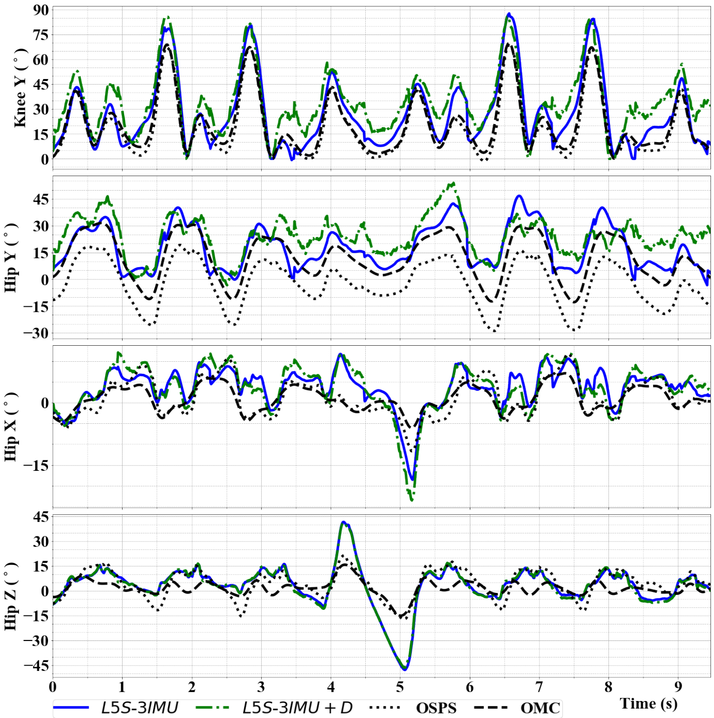

Figure 7. Knee (Y) and hip (Y, X, Z) joint angle output of *L5S-3IMU* in comparison with the benchmark system (Vicon) for a Walk trial. The subject walked straight from $t = 0$ to 3 s, turned 180° around from $t = 3$ to 5.5 s, and walked straight to the original starting point from 5.5 s until the end.

Table 4. Total travelled distance (TTD) deviation from optical motion capture (OMC) system at the ankles.

Algo.	Side	TTD Error % dev	Stride length (cm) Actual μ	med	Error $\mu \pm \sigma$	RMS	Gait speed (cm.s⁻1) Actual μ	med	Error $\mu \pm \sigma$	RMS
Freewalk	L	8.97%	91	99	-8.1 ± 6	9.9	70	74	-6.0 ± 5	7.7
L5S-3IMU	R	9.00%	93	99	-8.3 ± 6	10.3	71	75	-6.2 ± 5	8.2
Freewalk	L	5.23%	91	99	-4.7 ± 7	8.3	70	74	-3.6 ± 6	6.6
L5S-3IMU+D	R	5.85%	93	99	-5.4 ± 8	9.4	71	75	-4.1 ± 6	7.4
Jog	L	21.35%	81	86	-17.4 ± 23	28.5	107	118	-19.2 ± 33	38.0
L5S-3IMU	R	26.79%	85	97	-22.9 ± 25	33.8	111	124	-26.4 ± 34	43.1
Jog	L	22.40%	81	86	-18.2 ± 22	28.4	107	118	-21.6 ± 30	37.0
L5S-3IMU+D	R	26.70%	85	97	-22.8 ± 24	32.8	111	124	-27.5 ± 31	41.4
TUG	L	18.20%	74	76	-13.5 ± 18	22.1	58	60	-10.0 ± 15	18.0
L5S-3IMU	R	20.98%	79	90	-16.6 ± 15	22.5	63	67	-13.1 ± 13	18.4
TUG	L	3.80%	74	76	-2.8 ± 6	6.7	58	60	-2.3 ± 5	5.9
L5S-3IMU+D	R	4.22%	79	90	-3.3 ± 6	6.8	63	67	-2.7 ± 5	5.6

where μ and σ denote mean and standard deviation. Error denotes estimate minus actual value, while TTD % dev denotes abs$(error)$/actual TTD.

Preprints (www.preprints.org) | NOT PEER-REVIEWED | Posted: 3 November 2020 doi:10.20944/preprints202011.0166.v1

6.1. Mean Position and Orientation RMSE

The mean position and orientation RMSE of *L5S-3IMU*, *L5S-3IMU+D*, and related literature (sparse orientation poser (*SOP*) and sparse inertial poser (*SIP*) [12]) are listed in Table 5. *SOP* used orientation measured by IMUs and biomechanical constraints, while *SIP* used similar information but with the addition of acceleration. Both *SOP* and *SIP* were benchmarked against an OSPS system tracking the full body while our algorithm was benchmarked against an OMC system tracking only the lower body. The e_{pos} and e_{ori} (no bias) performance of *L5S-3IMU* and compared to *SOP* for free walking and jogging were comparable ($\Delta e_{pos} 0.1 - 0.5$ cm and $\Delta e_{ori} 2.5 - 3°$ differences). The e_{pos} and e_{ori} (no bias) of *SIP* was better than *L5S-3IMU* and *L5S-3IMU+D* for free walking (~$2.1 - 2.5$ cm and $6.5 - 7°$ difference). Although this improvement was expected, as *SIP* optimizes the pose over multiple frames whereas our algorithm, like *CKF-3IMU*, optimizes the pose for each individual frame. For jumping jacks, the e_{ori} of *L5S-3IMU* and *L5S-3IMU+D* was significantly (~$4 - 8°$) better than *SOP*'s and *SIP*'s. However, this difference is probably because both *SOP* and *SIP* were evaluated on the full body (our algorithm was only evaluated on the lower body) and errors in arm pose estimation may have increased e_{ori} for the *SOP* and *SIP* algorithms.

Table 5. Mean position and orientation RMSE of *L5S-3IMU*, *L5S-3IMU+D*, *OSPS*, Sparse orientation power (*SOP*) and Sparse inertial poser (*SIP*) [12].

	e_{pos} (cm)			e_{ori}, no bias (cm)		
	Free walk	Jog	Jumping jacks	Free walk	Jog	Jumping jacks
L5S-3I	5.1 ± 1.2	7.3 ± 1.4	8.7 ± 1.6	$17.5 \pm 2.7°$	$20.2 \pm 3.8°$	$12.8 \pm 4.0°$
L5S-3I + D	5.5 ± 1.0	6.2 ± 1.1	4.9 ± 0.9	$18.0 \pm 2.5°$	$17.4 \pm 3.2°$	$12.6 \pm 3.2°$
OSPS	5.4 ± 1.5	5.6 ± 1.2	5.5 ± 1.6	$12.9 \pm 4.0°$	$10.3 \pm 1.8°$	$7.6 \pm 3.3°$
SOP [12]	~5.0	~8.0	~8.0	~15.0°	~22.0°	~20.0°
SIP [12]	~3.0	~5.0	~4.0	~11.0°	~16.0°	~16.0°

Comparing processing times, *L5S-3IMU* and *L5S-3IMU+D* were slower than *CKF-3IMU*, but can still be used in real-time; specifically, *CKF-3IMU*, *L5S-3IMU*, and *L5S-3IMU+D* processed a 1,000-frame sequence (i.e., 10 seconds long) in ~0.7, ~2, ~3.5 seconds, respectively, on an Intel Core i5-6500 3.2 GHz CPU [9], while *SIP* [12] took 7.5 minutes on a quad-core Intel Core i7 3.5 GHz CPU. All set-ups used single-core non-optimized Matlab code. Albeit slower than *CKF-3IMU*, *L5S-3IMU* and *L5S-3IMU+D* could also be used to provide real-time gait parameter measurement to inform actuation of assistive or rehabilitation robotic devices.

6.2. Hip and Knee Joint Angle RMSE and CC

The knee and hip joint angle RMSEs (no bias) and CCs of *L5S-3IMU*, *L5S-3IMU+D*, *OSPS* and related literature for straight walking (i.e., per step evaluation) are shown in Table 6 [9,32–34]. Similar to IMC based systems, *L5S-3IMU* and *L5S-3IMU+D* also follows the trend of having sagittal (Y axis) joint angles similar to that captured by OMC systems (0.95 knee Y and > 0.83 hip Y CCs), but with significant difference in frontal and transverse (X and Z axis) joint angles [9,32]. *CKF-3IMU* performed slightly better (e.g., 0.03 knee Y, 0.09 hip Y CC), which is expected as the biomechanical constraint (i.e., no-knee-bending) assumption of *CKF-3IMU* was designed specifically for walking, at the cost of being less accurate for other dynamic movements. Both *L5S-3IMU* and *L5S-3IMU+D* were comparable, and at times even better (within 2.5° RMSE, 0.1 CC difference) than the results of Hu *et al.* and Tadano *et al.*, indicating excellent per-step reconstruction in the sagittal plane [33,34]. Hu *et al.* used 4 IMUs (two at the pelvis and one on each foot) and Tadano *et al.* used an OSPS configuration. Both systems can only estimate the pose in the sagittal plane.

Despite the promising performance when using inter-IMU distance measurements, further validation with actual hardware implementation is needed, as the sensor noise in the real world may not necessarily follow a normal distribution and may be non-stationary. For reference, portable

Preprints (www.preprints.org) | NOT PEER-REVIEWED | Posted: 3 November 2020 doi:10.20944/preprints202011.0166.v1

Table 6. Knee and hip angle RMSE no bias (top) and CC (bottom) of *CKF-3IMU*, *OSPS*, and related literature for free walk.

Joint angle RMSE (°)	Knee sagittal	Hip sagittal	Hip frontal	Hip transverse
L5S-3IMU	7.6 ± 2.6	6.6 ± 2.7	5.0 ± 2.6	8.6 ± 3.6
L5S-3IMU+D	7.1 ± 2.1	7.5 ± 2.1	5.1 ± 2.3	8.9 ± 3.7
OSPS	5.0 ± 1.8	3.6 ± 1.7	4.1 ± 2.2	11.9 ± 4.3
CKF-3IMU [9]	5.7 ± 2.2	4.4 ± 1.9	5.5 ± 2.6	9.0 ± 3.8
Cloete *et al*.[32]	8.5 ± 5.0	5.8 ± 3.8	7.3 ± 5.2	7.9 ± 4.9
Hu *et al*.[33]	4.9 ± 3.5	6.8 ± 3.0	-	-
Tadano *et al*.[34]	10.1 ± 1.0	7.9 ± 1.0	-	-
Joint angle CC	**Knee sagittal**	**Hip sagittal**	**Hip frontal**	**Hip transverse**
L5S-3IMU	0.95 ± 0.03	0.87 ± 0.16	0.76 ± 0.18	0.36 ± 0.36
L5S-3IMU+D	0.95 ± 0.03	0.83 ± 0.14	0.72 ± 0.19	0.29 ± 0.37
OSPS	0.97 ± 0.04	0.95 ± 0.06	0.72 ± 0.19	0.26 ± 0.20
CKF-3IMU [9]	0.98 ± 0.03	0.96 ± 0.08	0.73 ± 0.17	0.26 ± 0.39
Cloete *et al*.[32]	0.89 ± 0.15	0.94 ± 0.08	0.55 ± 0.40	0.54 ± 0.20
Hu *et al*.[33]	0.95 ± 0.04	0.97 ± 0.04	-	-
Tadano *et al*.[34]	0.97 ± 0.02	0.98 ± 0.01	-	-

ultrasound-based distance measurement can achieve millimetre accuracy with a sampling rate of 125 Hz [25], while a commercial UWB-based distance measurement devices can achieve ~10 cm accuracy with a sampling rate of 200 Hz [35,36].

Lastly, despite *L5S-3IMU* and *L5S-3IMU+D* achieving 0.95 joint angle CCs in the sagittal plane, the unbiased joint angle RMSE ($> 5°$) makes its utility in clinical applications uncertain [37]. Although the algorithm is expected to work on pathological gait where our biomechanical assumptions are satisfied, overall performance still needs more improvement. To achieve clinical utility, one may either use more accurate sensors or average out cycle-to-cycle variation in estimation errors over many gait cycles; for example, use a more accurate distance measurement sensor ($\sigma_{dist} < 0.1$ m). The evaluation of how these solutions can bridge the gap to clinical application for the proposed system will be part of future work.

6.3. Spatiotemporal Gait Parameters

The focus of the proposed algorithms, *L5S-3IMU* and *L5S-3IMU+D*, are to estimate joint kinematics. However, as *L5S-3IMU* and *L5S-3IMU+D* both track the global position of the ankles, it is also capable of calculating spatiotemporal gait parameters (performance listed in Table 4). The TTD deviation of our algorithms compared against the gold standard OMC were not as good as *CKF-3IMU* [9] (3.6 - 3.81% TTD deviation) or other state-of-the-art dead reckoning algorithms [38,39] (0.2 - 1.5% TTD deviation). Two possible sources of inaccuracy lies (1) in the dead reckoning approximation done in the prediction step, and (2) in the assumption that the velocity of the shank IMU is zero when the associated foot touches the floor, but of course this IMU continues to move with some small velocity on the lower shank during the stance phase. To illustrate the dead reckoning approximation, let us look at the predicted pelvis pose in Eq. (73). In our algorithm, we assumed $\boldsymbol{\psi}_p \approx \mathbf{I}_{3\times3}$ (note that $\Phi(-\Delta t\, {}^p\breve{\omega}_k) \approx \mathbf{I}_{3\times3}$ and $\tilde{\boldsymbol{R}}^{p+}_{k-1}(\breve{\boldsymbol{R}}^p_k)^T \approx \mathbf{I}_{3\times3}$ since $\Delta t\, {}^p\breve{\omega}_k$ is small) which did not significantly affect the

Preprints (www.preprints.org) | NOT PEER-REVIEWED | Posted: 3 November 2020 doi:10.20944/preprints202011.0166.v1

joint kinematic estimate, but slightly affected the global position estimate. Nevertheless, body drift has been reduced substantially compared to Marcard *et al.*'s *SIP* [12].

$$\begin{aligned} \hat{\boldsymbol{T}}_k^{p-} &= \tilde{\boldsymbol{T}}_{k-1}^{p+} \exp([\begin{bmatrix} (\breve{\boldsymbol{R}}_k^p)^T (\Delta t\, \tilde{\boldsymbol{v}}_{k-1}^{mp+} + \frac{\Delta t^2}{2}\, \breve{\boldsymbol{a}}_k^p) \\ \Delta t\, {}^p\breve{\boldsymbol{\omega}}_k \end{bmatrix}]^\wedge) \\ &= \begin{bmatrix} \tilde{\boldsymbol{R}}_{k-1}^{p+} \exp([\Delta t\, {}^p\breve{\boldsymbol{\omega}}_k]^\wedge) & \tilde{\boldsymbol{p}}_{k-1}^{mp+} + \overbrace{\tilde{\boldsymbol{R}}_{k-1}^{p+} \Phi(-\Delta t\, {}^p\breve{\boldsymbol{\omega}}_k)(\breve{\boldsymbol{R}}_k^p)^T}^{\boldsymbol{\psi}_p \approx \mathbf{I}_{3\times 3}} (\Delta t\, \tilde{\boldsymbol{v}}_{k-1}^{mp+} + \frac{\Delta t^2}{2}\, \breve{\boldsymbol{a}}_k^p) \\ \mathbf{0}_{1\times 3} & 1 \end{bmatrix} \end{aligned} \tag{73}$$

6.4. Limitations and Future Work

L5S has similar pelvis drift, covariance matrix numerical issue, and flat floor limitation as *CKF-3IMU*, which is expected as *L5S* implements the same measurement and constraint update as *CKF-3IMU*, albeit formulated using Lie group representation instead of vectors and quaternions [9]. The pelvis height and flat floor assumption helps prevent the pelvis and the ankles from drifting towards each other (i.e., pelvis drift downward while ankles drift upward). However, it will also prevent accurate pose estimation of motions such as sitting, lying down, or standing on one leg, where the pose is maintained for a duration much longer than that of a typical gait cycle. The covariance limiter (Sec. 3.2.2) helps prevent the covariance becoming badly conditioned (i.e., singular), especially for longer duration trials (e.g., *5-minute walk*) where the position uncertainty grows at a faster rate for the pelvis position than the ankle position. As can be observed from Fig. 6, substituting the pelvis height assumption with inter-IMU distance measurements can increase the algorithm's accuracy especially for tracking dynamic movements. If the distance measurement is accurate enough (i.e., smaller σ_{dist}^2), the inter-IMU distance measurement update may be enough to limit the growth of pelvis position uncertainly and possibly making the covariance limiter not needed.

Fig. 6 shows that the optimized performance of *L5S-3IMU*, even if it allows the tracked orientation to be corrected by inter-IMU distance measurements and the tracked position estimate, was only slightly better than *CKF-3IMU*/*L5S-3I-NO*, which effectively assumed the measurement input from the orientation estimation algorithm to be perfect (i.e., trusted the tracked orientation less). As *L5S-3IMU* requires more computing resources, such result suggests that *CKF-3IMU* may be more suitable to use when computing power is limited. To fully leverage the advantages brought by the Lie group representation, additional sensor measurements that can help correct tracked orientation will be needed (e.g., estimating angle of arrival between two sensors [40] or using fish eye cameras to improve pose estimate [41]).

Additional sensor measurements provide new opportunities for automatic calibration even under RSC configuration. IMC systems typically need anthropometric measurements (i.e., measurement of body segments such as d^{ls}) beforehand. By taking the initial distance measurement at some predetermined posture, anthropometric measurements can be automatically inferred. The formulation for a hinge joint with two IMUs on both sides has been leveraged to enable automatic sensor-to-segment calibration (i.e., align sensor frame to body frame) and even a completely magnetometer free orientation estimation [42,43]. Magnetometer free orientation estimation rids us of the yaw offset issue from an inhomogeneous magnetic field in indoor environments, typically with stronger disturbances closer to the floor [44]. An approach using a hinge joint with two IMUs may not be applicable to RSC configurations (e.g., our algorithm only has one IMU on one side of the hinge joint). However, distance measurements may be use to compensate for the missing IMU information from the uninstrumented segment, and a modified version may be developed for a RSC configuration.

Enabling longer-term tracking of ADL in the subject's natural environment may lead to novel investigations of movement disorder progression and the identification of early intervention opportunities. This work is just one of the early steps towards seamless remote gait monitoring. Developing solutions to further increase accuracy, increase the number of body segments tracked (e.g.,

Preprints (www.preprints.org) | NOT PEER-REVIEWED | Posted: 3 November 2020 doi:10.20944/preprints202011.0166.v1

track full body under RSC [12]), or use even fewer IMUs (tracking lower body using two IMUs [45]) will be investigated in the future.

7. Conclusions

This paper presented a Lie group CEKF-based algorithm (*L5S-3IMU*) to estimate lower limb kinematics using a RSC configuration of IMUs, supplemented by inter-IMU distance measurements in one implementation. The knee and hip joint angle RMSEs in the sagittal plane for straight walking were $7.6 \pm 2.6°$ and $6.6 \pm 2.7°$, respectively, while the CCs were 0.95 ± 0.03 and 0.87 ± 0.16, respectively. We also showed that inter-IMU distance measurement is a promising new source of information to improve the pose estimation of IMC under a RSC configuration. Simulations show that performance improved dramatically for dynamic movements even at higher noise levels (e.g., $\sigma_{dist} = 0.2$ m), and that similar performance to *L5S-3IMU* was achieved at $\sigma_{dist} = 0.1$ m for free walk movements. However, further validation is recommended with actual distance measurement from real sensors. The source code for the *L5S* algorithm, supplementary material, and links to sample videos will be made available at https://git.io/JTRQ3.

Author Contributions: conceptualization, L.S.; methodology, L.S.; software, L.S.; validation, L.S.; formal analysis, L.S. and S.R.; investigation, L.S.; resources, S.R and N.L; data curation, L.S.; writing–original draft preparation, L.S.; writing–review and editing, L.S., S.R., and N.L.; visualization, L.S.; supervision, S.R. and N.L.; project administration, S.R.

Funding: This research received no external funding.

Acknowledgments: This research was supported by an Australian Government Research Training Program (RTP) Scholarship.

Conflicts of Interest: The authors declare no conflict of interest.

Abbreviations

The following abbreviations are used in this manuscript:

OMC	Optical Motion Capture
IMC	Inertial Motion Capture
IMU	Inertial Measurement Unit
OSPS	One Sensor per Body Segment
RSC	Reduced-Sensor-Count
KF	Kalman Filter
CEKF	Constrained Extended Kalman Filter
ADL	Activities of Daily Living
TTD	Total Travelled Distance
SOP	Sparse Orientation Poser
SIP	Sparse Inertial Poser

Appendix A Derivation of Pelvis-to-Ankle Distance Measurement

This section explains the derivation of the measurement pelvis-to-ankle vector (Eq. (46)) as obtained from pelvis-to-ankle distance measurements, $\breve{d}_k^{pla}$ and $\breve{d}_k^{pra}$, while assuming hinged knee joints and constant body segment lengths. For the sake of brevity, only the left side formulation is shown. The right side (i.e., pelvis to right ankle vector) can be calculated similarly.

First, we solve for an estimated left knee angle, $\hat{\theta}_k^{lk}$ (Eq. (47)), from the measured pelvis to left ankle distance, $\breve{d}_k^{pla}$. The pelvis to left ankle vector, $\tau_m^{pla}(\hat{\boldsymbol{\mu}}_k^-, \theta_k^{lk})$ (Eq. (A6)), can be defined as the sum of the mid-pelvis to hip, thigh long axis, and shank long axis vectors.

$$\tau_{pla}(\hat{\boldsymbol{\mu}}_k^-, \theta_k^{lk}) = \overbrace{\frac{d^p}{2}\, \hat{\boldsymbol{T}}_k^{p-}\, \boldsymbol{i}_y - d^{ls}\, \hat{\boldsymbol{T}}_k^{ls-}\, \boldsymbol{i}_z}^{\boldsymbol{\psi}_{pla} = \text{half pelvis } y\text{-axis + shank } z\text{-axis}} + \overbrace{d^{lt}\, \hat{\boldsymbol{T}}_k^{ls-}(\boldsymbol{i}_x \sin(\theta_k^{lk}) - \boldsymbol{i}_z \cos(\theta_k^{lk}))}^{\text{thigh } z\text{-axis in shank frame}} \tag{A1}$$

 doi:10.20944/preprints202011.0166.v1

By definition of $(\check{d}_k^{pla})^2$ and expanding $\tau_m^{pla}(\hat{\boldsymbol{\mu}}_k^-, \theta_k^{lk})$ with Eq. (A1), we obtain

$$\begin{aligned}(\check{d}_k^{pla})^2 &= (\tau_{pla}(\hat{\boldsymbol{\mu}}_k^-, \theta_k^{lk}))^T\, \tau_{pla}(\hat{\boldsymbol{\mu}}_k^-, \theta_k^{lk}) \\ &= \boldsymbol{\psi}_{pla}^T \boldsymbol{\psi}_{pla} - 2d^{lt} \boldsymbol{\psi}_{pla}^T\, \hat{\boldsymbol{T}}^{ls-}\, \boldsymbol{i}_z \cos(\theta_k^{lk}) + 2d^{lt} \boldsymbol{\psi}_{pla}^T\, \hat{\boldsymbol{T}}^{ls-}\, \boldsymbol{i}_x \sin(\theta_k^{lk}) + (d^{lt})^2\end{aligned} \tag{A2}$$

Eq. (A2) can be rearranged in the form of Eq. (A3) with α, β, γ as shown in Eq. (A4).

$$\alpha \cos(\theta_k^{lk}) + \beta \sin(\theta_k^{lk}) = \gamma \tag{A3}$$

$$\alpha = -2d^{lt} \boldsymbol{\psi}_{pla}^T\, \hat{\boldsymbol{T}}_k^{ls-}\, \boldsymbol{i}_z, \quad \beta = 2d^{lt} \boldsymbol{\psi}_{pla}^T\, \hat{\boldsymbol{T}}_k^{ls-}\, \boldsymbol{i}_x, \quad \gamma = (\check{d}_k^{pla})^2 - \boldsymbol{\psi}_{pla}^T \boldsymbol{\psi}_{pla} - (d^{lt})^2 \tag{A4}$$

Solving for $\hat{\theta}_k^{lk}$ from Eq. (A3) gives us a quadratic equation with two solutions as shown in Eqs. (A5) and (47). Between the two solutions, $\hat{\theta}_k^{lk}$ is set as the $\hat{\theta}_k^{lk}$ whose value is closer to the current left knee angle estimate from the prediction step. This solution serves as a pseudomeasurement of the knee angle.

$$\hat{\theta}_k^{lk} = \cos^{-1}\left(\frac{\alpha\gamma \pm \beta\sqrt{\alpha^2+\beta^2-\gamma^2}}{\alpha^2+\beta^2}\right) \tag{A5}$$

Finally, $\mathbf{Z}_{pla,k}$, the KF measurement shown in Eqs. (A6) and (46), is the inter-IMU vector between the pelvis and left ankle, calculated using Eq. (A1) with input $\hat{\theta}_k^{lk}$.

$$\mathbf{Z}_{pla,k} = \tau_m^{pla}(\hat{\boldsymbol{\mu}}_k^-, \hat{\theta}_k^{lk}) \tag{A6}$$

References

1. Lloréns, R.; Gil-Gómez, J.A.; Alcañiz, M.; Colomer, C.; Noé, E. Improvement in balance using a virtual reality-based stepping exercise: A randomized controlled trial involving individuals with chronic stroke. *Clinical Rehabilitation* **2015**, *29*, 261–268.
2. Shull, P.; Lurie, K.; Shin, M.; Besier, T.; Cutkosky, M. Haptic gait retraining for knee osteoarthritis treatment. 2010 IEEE Haptics Symposium. IEEE, 2010, pp. 409–416.
3. Roetenberg, D.; Luinge, H.; Slycke, P. Xsens MVN: Full 6DOF human motion tracking using miniature inertial sensors. *Xsens Motion Technologies BV, Tech. Rep* **2009**, *1*.
4. Del Rosario, M.B.; Lovell, N.H.; Redmond, S.J. Quaternion-based complementary filter for attitude determination of a smartphone. *IEEE Sensors Journal* **2016**, *16*, 6008–6017.
5. Del Rosario, M.B.; Khamis, H.; Ngo, P.; Lovell, N.H.; Redmond, S.J. Computationally efficient adaptive error-state Kalman filter for attitude estimation. *IEEE Sensors Journal* **2018**, *18*, 9332–9342.
6. Tautges, J.; Zinke, A.; Krüger, B.; Baumann, J.; Weber, A.; Helten, T.; Müller, M.; Seidel, H.; Eberhardt, B. Motion reconstruction using sparse accelerometer data. *ACM Transactions on Graphics (TOG)* **2011**, *30*, 18, [1006.4903].
7. Huang, Y.; Kaufmann, M.; Aksan, E.; Black, M.J.; Hilliges, O.; Pons-Moll, G. Deep inertial poser: Learning to reconstruct human pose from sparse inertial measurements in real time. SIGGRAPH Asia 2018 Technical Papers, SIGGRAPH Asia 2018. Association for Computing Machinery, Inc, 2018, [1810.04703].
8. Salarian, A.; Burkhard, P.R.; Vingerhoets, F.J.G.; Jolles, B.M.; Aminian, K. A novel approach to reducing number of sensing units for wearable gait analysis systems. *IEEE Transactions on Biomedical Engineering* **2013**, *60*, 72–77.
9. Sy, L.W.; Raitor, M.; Del Rosario, M.B.; Khamis, H.; Kark, L.; Lovell, N.H.; Redmond, S.J.; Rosario, M.D.; Khamis, H.; Kark, L.; Lovell, N.H.; Redmond, S.J. Estimating lower limb kinematics using a reduced wearable sensor count, [arXiv:cs.RO/1910.00910].
10. Lin, J.F.; Kulić, D. Human pose recovery using wireless inertial measurement units. *Physiological Measurement* **2012**, *33*, 2099–2115.
11. Meng, X.L.; Zhang, Z.Q.; Sun, S.Y.; Wu, J.K.; Wong, W.C. Biomechanical model-based displacement estimation in micro-sensor motion capture. *Measurement Science and Technology* **2012**, *23*, 055101.

Preprints (www.preprints.org) | NOT PEER-REVIEWED | Posted: 3 November 2020 doi:10.20944/preprints202011.0166.v1

12. von Marcard, T.; Rosenhahn, B.; Black, M.J.; Pons-Moll, G. Sparse inertial poser: Automatic 3D human pose estimation from sparse IMUs. Computer Graphics Forum. Wiley Online Library, 2017, Vol. 36, pp. 349–360, [1703.08014].
13. Barfoot, T.D. *State Estimation for Robotics*; Cambridge University Press, 2017.
14. Wang, Y.; Chirikjian, G.S. Error propagation on the Euclidean group with applications to manipulator kinematics. *IEEE Transactions on Robotics* **2006**, *22*, 591–602.
15. Barfoot, T.D.; Furgale, P.T. Associating uncertainty with three-dimensional poses for use in estimation problems. *IEEE Transactions on Robotics* **2014**, *30*, 679–693.
16. Bourmaud, G.; Mégret, R.; Arnaudon, M.; Giremus, A. Continuous-discrete extended Kalman filter on matrix Lie groups using concentrated Gaussian distributions. *Journal of Mathematical Imaging and Vision* **2014**, *51*, 209–228.
17. Brossard, M.; Bonnabel, S.; Condomines, J.P. Unscented Kalman filtering on Lie groups. IEEE International Conference on Intelligent Robots and Systems, 2017, Vol. 2017-Septe, pp. 2485–2491.
18. Ćesić, J.; Joukov, V.; Petrović, I.; Kulić, D. Full body human motion estimation on lie groups using 3D marker position measurements. *IEEE-RAS International Conference on Humanoid Robots* **2016**, pp. 826–833.
19. Joukov, V.; Cesic, J.; Westermann, K.; Markovic, I.; Petrovic, I.; Kulic, D. Estimation and observability analysis of human motion on Lie groups. *IEEE Transactions on Cybernetics* **2019**, pp. 1–12.
20. Joukov, V.; Cesic, J.; Westermann, K.; Markovic, I.; Kulic, D.; Petrovic, I. Human motion estimation on Lie groups using IMU measurements. *IEEE International Conference on Intelligent Robots and Systems* **2017**, *2017-Septe*, 1965–1972.
21. Hol, J.D.; Dijkstra, F.; Luinge, H.; Schöny, T.B.; Schon, T.B.; Schön, T.B. Tightly coupled UWB/IMU pose estimation. 2009 IEEE International Conference on Ultra-Wideband. IEEE, 2009, pp. 688–692.
22. Malleson, C.; Gilbert, A.; Trumble, M.; Collomosse, J.; Hilton, A. Real-time full-body motion capture from video and IMUs. *International Conference on 3D Vision (3DV)* **2017**.
23. Gilbert, A.; Trumble, M.; Malleson, C.; Hilton, A.; Collomosse, J. Fusing visual and inertial sensors with semantics for 3D human pose estimation. *International Journal of Computer Vision* **2019**, *127*, 381–397.
24. Helten, T.; Muller, M.; Seidel, H.P.; Theobalt, C. Real-time body tracking with one depth camera and inertial sensors. Proceedings of the IEEE International Conference on Computer Vision, 2013, pp. 1105–1112.
25. Vlasic, D.; Adelsberger, R.; Vannucci, G.; Barnwell, J.; Gross, M.; Matusik, W.; Popović, J. Practical motion capture in everyday surroundings. ACM Transactions on Graphics; ACM Press: New York, New York, USA, 2007; Vol. 26, p. 35.
26. Sy, L.; Lovell, N.H.; Redmond, S.J. Estimating lower limb kinematics using distance measurements with a reduced wearable inertial sensor count. *2020 42nd Annual International Conference of the IEEE Engineering in Medicine and Biology Society (EMBC)* **2020**, [2003.10228].
27. Sy, L.; Lovell, N.H.; Redmond, S.J. Estimating lower limb kinematics using a Lie group constrained EKF and a reduced wearable IMU count. 2020 8th IEEE International Conference on Biomedical Robotics and Biomechatronics (Biorob), 2020, [1910.01808v1].
28. Selig, J.M. Lie groups and Lie algebras in robotics. In *Computational Noncommutative Algebra and Applications*; Springer, 2004; pp. 101–125.
29. Stillwell, J. *Naive Lie theory*; Springer Science & Business Media, 2008.
30. Chirikjian, G. *Stochastic models, information theory, and Lie groups. II: Analytic methods and modern applications*; 2012.
31. Bourmaud, G.; Megret, R.; Giremus, A.; Berthoumieu, Y. Discrete extended Kalman filter on Lie groups. European Signal Processing Conference, 2013, pp. 1–5.
32. Cloete, T.; Scheffer, C. Benchmarking of a full-body inertial motion capture system for clinical gait analysis. 2008 30th Annual International Conference of the IEEE Engineering in Medicine and Biology Society. IEEE, 2008, pp. 4579–4582.
33. Hu, X.; Yao, C.; Soh, G.S. Performance evaluation of lower limb ambulatory measurement using reduced inertial measurement units and 3R gait model. IEEE International Conference on Rehabilitation Robotics, 2015, pp. 549–554.
34. Tadano, S.; Takeda, R.; Miyagawa, H. Three dimensional gait analysis using wearable acceleration and gyro sensors based on quaternion calculations. *Sensors* **2013**, *13*, 9321–9343, [NIHMS150003].

 doi:10.20944/preprints202011.0166.v1

35. Malajner, M.; Planinsic, P.; Gleich, D. UWB ranging accuracy. 2015 22nd International Conference on Systems, Signals and Image Processing - Proceedings of IWSSIP 2015, 2015, pp. 61–64.
36. Ledergerber, A.; D'Andrea, R. Ultra-wideband range measurement model with Gaussian processes. 1st Annual IEEE Conference on Control Technology and Applications, CCTA 2017, 2017, Vol. 2017-Janua, pp. 1929–1934.
37. McGinley, J.L.; Baker, R.; Wolfe, R.; Morris, M.E. The reliability of three-dimensional kinematic gait measurements: A systematic review. *Gait and Posture* **2009**, *29*, 360–369.
38. Jimenez, A.R.; Seco, F.; Prieto, J.C.; Guevara, J. Indoor Pedestrian navigation using an INS/EKF framework for yaw drift reduction and a foot-mounted IMU. *Proceedings of the 2010 7th Workshop on Positioning, Navigation and Communication, WPNC'10* **2010**, pp. 135–143.
39. Zhang, W.; Li, X.; Wei, D.; Ji, X.; Yuan, H. A foot-mounted PDR System Based on IMU/EKF+HMM+ZUPT+ZARU+HDR+compass algorithm. *2017 International Conference on Indoor Positioning and Indoor Navigation, IPIN 2017* **2017**, *2017-Janua*, 1–5.
40. Dotlic, I.; Connell, A.; Ma, H.; Clancy, J.; McLaughlin, M. Angle of arrival estimation using decawave DW1000 integrated circuits. *2017 14th Workshop on Positioning, Navigation and Communications, WPNC 2017* **2018**, *2018-Janua*, 1–6.
41. Xu, W.; Chatterjee, A.; Zollh, M.; Rhodin, H.; Fua, P.; Seidel, H.p.; Theobalt, C. Mo2Cap2 : Real-time mobile 3D motion capture with a cap-mounted fisheye camera. *IEEE Transactions on Visualization and Computer Graphics (Proc. IEEE VR, 2019)* **2019**, *25*, 2093–2101.
42. Laidig, D.; Schauer, T.; Seel, T. Exploiting kinematic constraints to compensate magnetic disturbances when calculating joint angles of approximate hinge joints from orientation estimates of inertial sensors. *IEEE International Conference on Rehabilitation Robotics* **2017**, pp. 971–976.
43. Eckhoff, K.; Kok, M.; Lucia, S.; Seel, T. Sparse magnetometer-free inertial motion tracking – A condition for observability in double hinge joint systems, [2002.00902].
44. de Vries, W.H.; Veeger, H.E.; Baten, C.T.; van der Helm, F.C. Magnetic distortion in motion labs, implications for validating inertial magnetic sensors. *Gait and Posture* **2009**, *29*, 535–541.
45. Li, T.; Wang, L.; Li, Q.; Liu, T. Lower-body walking motion estimation using only two shank-mounted inertial measurement units (IMUs). *IEEE/ASME International Conference on Advanced Intelligent Mechatronics, AIM* **2020**, *2020-July*, 1143–1148.